LOW-MASS STAR FORMATION AND THE INITIAL MASS FUNCTION IN THE ρ OPHIUCHI CLOUD CORE[1]

K. L. LUHMAN[2] AND G. H. RIEKE

Steward Observatory, University of Arizona, Tucson, AZ 85721; kluhman@as.arizona.edu, grieke@as.arizona.edu

ABSTRACT

We have obtained moderate-resolution ($R = 800$–1200) K-band spectra for ~ 100 stars within and surrounding the cloud core of ρ Oph. We have measured spectral types and continuum veilings and have combined this information with results from new deep imaging. Using the latest evolutionary tracks of D'Antona & Mazzitelli to interpret the H-R diagram for ρ Oph, we infer ages ranging between 0.1 and 1 Myr for the class II and III sources (i.e., those that have emerged from their natal cocoons). A few stars may be slightly older. The initial mass function (IMF) peaks at about 0.4 $M_\odot$ and slowly declines to the hydrogen-burning limit with a slope of ~ -0.5 in logarithmic units (Salpeter is $+1.35$). Our lower limits on the numbers of substellar objects demonstrate that the IMF probably does not fall more steeply below the hydrogen-burning limit, at least down to ~ 0.02 $M_\odot$. The derived IMF is consistent with previous findings that the ρ Oph IMF is roughly flat from 0.05 to 1 $M_\odot$. The exact shape of the mass function remains a function of the theoretical evolutionary tracks and, at the lowest masses, the conversion from spectral types to effective temperatures. We then make the first comparison of mass functions of stars and prestellar clumps measured in the same region. The similar behavior of the two mass functions in ρ Oph supports the suggestion of Motte et al. and Testi & Sargent that the stellar mass function in young clusters is a direct product of the process of cloud fragmentation. We have also studied the very young and often still embedded class I and flat-spectrum objects. After considering the effect of extinction on the SED classifications of the sample, we find that $\sim 17\%$ of the ρ Oph stars are class I, implying ~ 0.1 Myr for the lifetime of this stage. In spectra separated by 2 yr, we observe simultaneous variability in the Brγ emission and K-band continuum veiling for two stars, where the hydrogen emission is brighter in the more heavily veiled data. This behavior indicates that the disk may contribute significantly to continuous K-band emission, in contrast to the proposal that the infalling envelope always dominates. Our detection of strong 2 μm veiling ($r_K = 1$–4) in several class II and III stars, which should have disks but little envelope material, further supports this proposition. We also detect absorption features in the spectra of $\sim 25\%$ of class I and flat-spectrum sources, demonstrating the feasibility of studying the photospheres of extremely young protostars.

Subject headings: infrared: stars — open clusters and associations: individual (ρ Ophiuchi) — stars: evolution — stars: low-mass, brown dwarfs — stars: luminosity function, mass function — stars: pre–main-sequence

1. INTRODUCTION

The birth of low-mass stars and brown dwarfs as well as the evolution of circumstellar disks and planetary systems can best be studied in the nearest ($d < 500$ pc) young (age <10 Myr) stellar clusters and associations. For example, the distribution of masses in these populations directly reflects the initial mass function (IMF). In contrast, in regions such as the local field or globular clusters, the present-day mass function is the product of a complex evolution.

Until recently, these advantages of young clusters were difficult to exploit because of extinction. However, by complementing optical techniques with modern infrared (IR) imaging and spectroscopy, we can estimate luminosities and spectral types for complete, well-defined samples of young objects within obscured star-forming regions. Because of the luminous nature of newborn substellar objects, such

data can be converted to mass functions that reach below the hydrogen-burning limit.

The ρ Ophiuchi dark cloud core contains a very young (<1 Myr), nearby ($d = 160$ pc), compact ($D \sim 20'$) population of ~ 100 low-mass stars, making it ideal for IMF studies. Because of the large extinction within the cloud, optical spectral types and photometry (Bouvier & Appenzeller 1992; Martín et al. 1998) and soft X-ray data (Montmerle et al. 1983; Casanova et al. 1995) are available for only a small fraction of the stars. Until recently, the ρ Oph members were studied primarily through their near- to mid-IR spectral energy distributions (SEDs), which were observed with single element detectors on the ground and aboard the *IRAS* satellite (Elias 1978; Lada & Wilking 1984; Wilking, Lada, & Young 1989; Greene et al. 1994). Following the initial observations of ρ Oph with near-IR arrays (Barsony et al. 1989; Rieke, Ashok, & Boyle 1989), Greene & Young (1992) surveyed 650 arcmin² of the cloud at J, H, and K, providing a relatively sensitive ($K \sim 13$) photometric census of the stellar population. To reach young objects below the hydrogen-burning limit, Rieke & Rieke (1990) obtained deep images ($K \sim 15.5$) of 200 arcmin² within the cloud core ($A_V \gtrsim 50$; Wilking & Lada 1983) and identified several brown dwarf candidates. The

---

[2] Present address: Harvard-Smithsonian Center for Astrophysics, 60 Garden Street, Cambridge, MA 02138.

substellar nature of these sources has been supported by *ISO* mid-IR photometry (Comerón et al. 1998, hereafter CRCTL) and confirmed through spectroscopy in the optical (Luhman, Liebert, & Rieke 1997) and IR (Williams et al. 1995; Wilking, Greene, & Meyer 1998, hereafter WGM). Comerón et al. (1993, hereafter CRBR) supplemented the data of Rieke & Rieke (1990) with *JHKL'* aperture photometry of a complete sample of sources projected against the dense cloud core. They introduced a method of fitting the data to estimate individual source properties and deduced a logarithmically flat IMF (the Salpeter index is +1.35) down to and below the hydrogen-burning limit. Strom, Kepner, & Strom (1995) used an alternate approach introduced by Meyer (1995) that also indicated a flat IMF. Williams et al. (1995) showed that the techniques of CRBR and Strom et al. (1995) agree at the detailed level of individual source properties as well as overall IMF slope.

Following these photometric studies, near-IR spectroscopy has been applied in studying other properties of the embedded stellar population in ρ Oph. After measuring *K*-band spectral types for 19 stars ($K < 10.5$, $R = 500$), Greene & Meyer (1995) constructed a Hertzsprung-Russell (H-R) diagram in which the theoretical evolutionary tracks of D'Antona & Mazzitelli (1994, hereafter DM94) implied an age of ~ 0.5 Myr for the cluster. Greene & Lada (1996) also observed ~ 100 young stars in Taurus and ρ Oph ($R = 500$) with broader wavelength coverage (1.15–2.42 μm). The appearance of the spectra was closely correlated with SED class, indicating, as expected, that reddening increases and photospheric features weaken from class III to class I sources (Lada 1987) and thus confirming the previous conclusions drawn from spectroscopy of 2.3 μm CO absorption in young ρ Oph members (Casali & Matthews 1992). This trend is consistent with the large obscuration and strong continuum veiling expected from circumstellar material in the presumably younger, earlier SED classes. Finally, Casali & Eiroa (1996) and Greene & Lada (1997) used high-resolution spectra ($R = 17,000$ and 21,000, respectively) to measure continuum veilings and line widths for a small sample of flat-spectrum sources in ρ Oph and other young clusters. They demonstrated that the line profiles are consistent with absorption originating in very young stellar photospheres rather than circumstellar disks, an important result that supports the validity of our classification of young stellar populations through IR spectra.

In this paper, we expand on the previous IR spectral classification in ρ Oph and continue a program started in L1495E (Luhman & Rieke 1998, hereafter LR) and IC 348 (Luhman et al. 1998b, hereafter LRLL). We have obtained *K*-band spectroscopy of ~ 100 sources, combining a magnitude-limited sample in the cloud core ($K \lesssim 12$) with a representative population from the outer regions of the cluster ($K \lesssim 11$). The moderate spectral resolution ($R = 800$–1200) of the data allows both reasonably accurate spectral types (± 1–2 subclasses) and sensitivity to low-mass members of ρ Oph ($\geq 0.1\,M_\odot$). With the measured spectral types we construct an H-R diagram and use theoretical evolutionary tracks to derive an IMF and star formation history for the emerged members of the cluster (predominantly class II and III). Likely substellar cloud members examined by Luhman et al. (1997), WGM, and CRCTL are added to the mass function, extending the IMF to lower masses. We then use a new *K*-band luminosity function (KLF) of the cloud core to develop a model of the

reddened background population and identify likely cluster members lacking spectroscopy. After accounting for these sources, we arrive at an IMF complete to $\sim 0.08\,M_\odot$, which is compared to results from other young clusters.

Using the mid-IR photometry of previous authors, we revise the SED classifications of the ρ Oph population by dereddening the near- to mid-IR spectral indices with guidance from our near-IR spectra. With the new classifications, the relative numbers of sources in the different categories are consistent with expectations that the dust-embedded stage should have a very short duration. The broadband photometric data combined with the measurements of the *K*-band continuum veiling and Brγ emission present new constraints on the nature of the IR excess emission in young stars. In particular, simultaneous variability of Brγ emission and veiling is seen in two stars, possibly indicating the importance of disks as sources of 2 μm excess emission. In addition, we find that photospheric absorption features are detectable in a number of class I and flat-spectrum sources, while significant veiling is measured in several class II objects. Both the placements on the H-R diagram and the distributions of SED classes indicate a slight increase in average age between the cloud core and surrounding region.

2. OBSERVATIONS

We performed *K*-band spectroscopy on sources in ρ Oph using the near-IR long-slit spectrometer FSPEC (Williams et al. 1993) at the Steward 2.3 m Bok Reflector on Kitt Peak on 1994 July 15 and 1995 May 16, 17, and 19 and at the Multiple Mirror Telescope (MMT) on Mount Hopkins on 1994 July 2–3, 1996 May 28–31, and 1996 June 3–6. Most of the spectra were obtained in 1996 with a grating providing a 2 pixel resolution of $R = \lambda/\Delta\lambda = 1200$, while the data from 1994 and 1995 have a resolution of $R = 800$. The observations and data reduction procedures were identical to those described by LRLL. We selected for spectroscopy ~ 30 sources with $K \lesssim 12$ appearing in IR images of the cloud core by CRBR. With the addition of spectra from Williams et al. (1995), our sample contains ~ 40 sources and is nearly complete to $K = 12$. In the region surrounding the core and within Figure 1, we observed ~ 70 sources with $K \lesssim 11$ found in Greene & Young (1992). A few bright stars outside of the region in Figure 1 were also observed, taken from Wilking et al. (1989) and Greene et al. (1994).

The spatial distribution of the spectroscopic sample is illustrated in Figure 1 and the spectra are presented in Figures 2–6. Line identifications were made by comparison to the high-resolution ($R \geq 45,000$) spectra of cool stars obtained by Wallace & Hinkle (1996).

Imaging at K_s (1.9–2.3 μm) was performed at the Bok Reflector on the nights of 1998 April 12–15 using the Steward Observatory NICMOS3 256×256 near-IR camera at a plate scale of 0''.64 pixel^{-1}, corresponding to a total field of 2'.7 $\times$ 2'.7. In 43 pointings, we observed the same region covered by CRBR (*dashed lines* in Fig. 1), in addition to a few extra positions, for a total of ~ 250 arcmin^2. Follow-up observations were made with standard *J* and *H* during 1998 May 8–10 and July 14. We selected pointings that contained several faint, possibly low-luminosity *K*-band sources (*dotted lines* in Fig. 1). At each position, we obtained images with dithers of 5'' in a 4×4 grid, facilitating efficient flat fielding and removal of bad pixels. Each exposure consisted of two coadded 30 s frames,
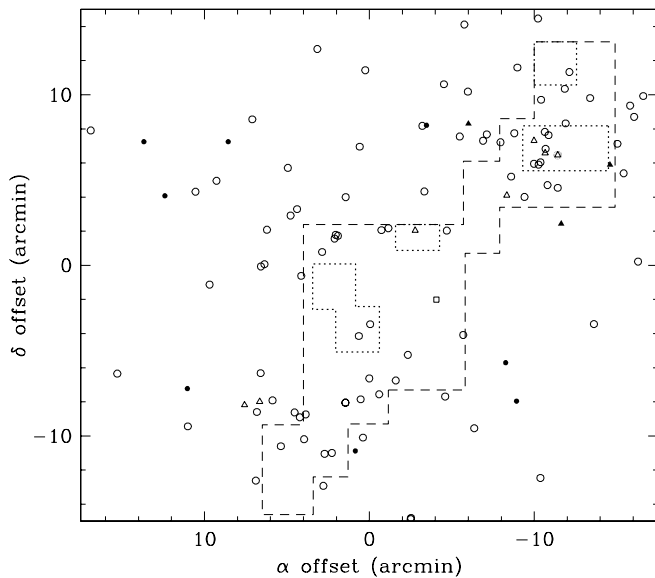
FIG. 1.—All sources in ρ Oph observed with K-band spectroscopy, with the exception of seven objects falling outside of this region (IRS 2, IRAS 64A, SR 22, WSB 38, WSB 45, WSB 46, and ROXs 39). Filled circles represent stars classified as background giants in this work, and open circles are all other sources in our sample. Open triangles and the open square are the additional low-mass objects observed spectroscopically by WGM and Luhman et al. (1997). Filled triangles are identified as likely background stars by WGM. The area within the dashed line was surveyed through IR images by CRBR and corresponds to the cloud core ($A_V \gtrsim 50$; Wilking & Lada 1983). Deeper K-band photometry of the same region was obtained for this work, in addition to J and H images toward the positions outlined by dotted lines. The origin corresponds to $\alpha = 16^h24^m07^s7$, $\delta = -24°24'00''$ (1950).

producing a total exposure time of 16 minutes. A flat field was constructed by median combining frames that lacked bright sources. For calibration, we observed a photometric standard star, SR 3, periodically during the night. These exposures were taken out of focus to guard against saturation. After dark-subtracting and flat-fielding the images, the 16 frames at a given position were shifted and combined into one image. The tasks DAOFIND and PHOT under the package APPHOT were used in measuring the stellar coordinates and extracting photometry. The density of stars was low enough that we could measure the background emission in an annulus around each star and subtract it from the photometry. The data were calibrated with the CIT photometry of SR 3 from Elias et al. (1982) and are essentially in the CIT system. The K images are complete to $K \sim 17$, based both on the detection of many sources down to $K = 17.5$ and, more importantly, and on the fact that the background source counts do not deviate from the expected behavior until $K > 17$ (see § 4.3.2). Using the coordinates measured by Barsony et al. (1997, hereafter BKLT) for stars above their detection limit ($K < 14.5$) and below our saturation limit ($K > 10$), we derived relatively precise ($\pm 1''$) coordinates for the fainter sources ($K > 14.5$).

3. INDIVIDUAL SOURCE CHARACTERISTICS

3.1. Spectral Types

The spectral types derived for the ρ Oph sample are listed in Table 1, along with measurements of Brγ emission and continuum veiling at 2.2 μm [$r_K = I_{2.2}$(IR excess)/$I_{2.2}$(star)]. Typical uncertainties are 0.25–0.5 in r_K, depending on the signal-to-noise ratio, spectral type, and degree of

veiling. Most of the objects in our sample have been classified by the metallic absorption lines appearing in the K-band spectra, as described in § 3.1.1. In our K-band sample, we include all additional data obtained by Williams et al. (1995) (GY 5, GY 10, GY 37, GY 202, and 162618−242611). A total of 40 sources from this combined spectroscopic sample fall within the cloud core. We have adopted the spectral type of WGM for one of these (162618−242416) and now refer to it as part of the WGM sample. In § 3.1.2, we derive spectral types from the steam absorption in these spectra and compare our results to those of WGM. We revise the classifications of WGM for objects not in our sample to correct for a possible systematic error due to gravity dependence of the steam band strength. Comments on the individual sources are given in the Appendix. The optical classification of the brown dwarf GY 141 (Luhman et al. 1997) is also included in Table 1.

3.1.1. IR Spectral Classification of the New Sample

In a study of the small stellar aggregate in L1495E in Taurus, LR developed a technique of K-band spectral classification ($R \sim 1000$) to derive the spectral types and continuum veilings of young, late-type stars (~ 1 Myr, $> G0$). This method was then used to classify ~ 100 stars in IC 348, where the optical and IR spectral types were in reasonable agreement. The subtleties of K-band classification of young stars are discussed by LR and LRLL. For instance, the surface gravity of pre–main-sequence stars is intermediate between that of dwarfs and giants, resulting in weakened Na absorption at both 2.2 μm and 8200 Å in young M stars relative to M dwarfs (Luhman et al. 1998a; Martín, Rebolo, & Zapatero Osorio 1996). Comparing the data obtained in IC 348 ($R = 800$) and that presented here ($R = 1200$), we find that the higher resolution provides more accurate spectral types for G through M stars while maintaining sensitivity to faint sources. At higher resolution we obtain more accurate measurements of Mg at 2.28 μm, as illustrated in the observations of GY 240A, GY 240B, and GY 250 at $R = 800$ and 1200 (Figs. 2, 3, and 4). The strength of Mg relative to Ca is important in the spectral classification of K through mid-M stars. Mg becomes weaker with later spectral type and eventually disappears beyond M2. For mid-M and later, two other features (Ca and an unidentified line) appear near 2.28 μm and can be mistaken for Mg when blended together at $R < 1000$. The two lines are resolved at $R \geq 1200$, allowing a more accurate classification (see V410 Tau X-ray 6 in Fig. 3).

The new spectra are shown in Figures 2–6 in order of spectral type and veiling. Background giants have very distinct spectra and are relatively easy to classify in moderate signal-to-noise ratio data. A few spectra of lower quality are also shown, where the strong CO absorption could arise in either background giants or late-type cluster members. The spectral slopes, atomic line strengths, and mid-IR emission excesses imply that most of these objects are probably the latter. Given the various effects of veiling, surface gravity, and temperature on the appearance of these spectra, degeneracies in the classifications can occur. For instance, the sources classified as M4 are also matched by late-K stars with atomic lines weakened by veiling and CO enhanced by low gravity. After comparison of IR and optical types in IC 348, we find that generally the simplest IR classification is the appropriate one, rather than a spectral type that requires simultaneous veiling and strengthening of CO. Pre-
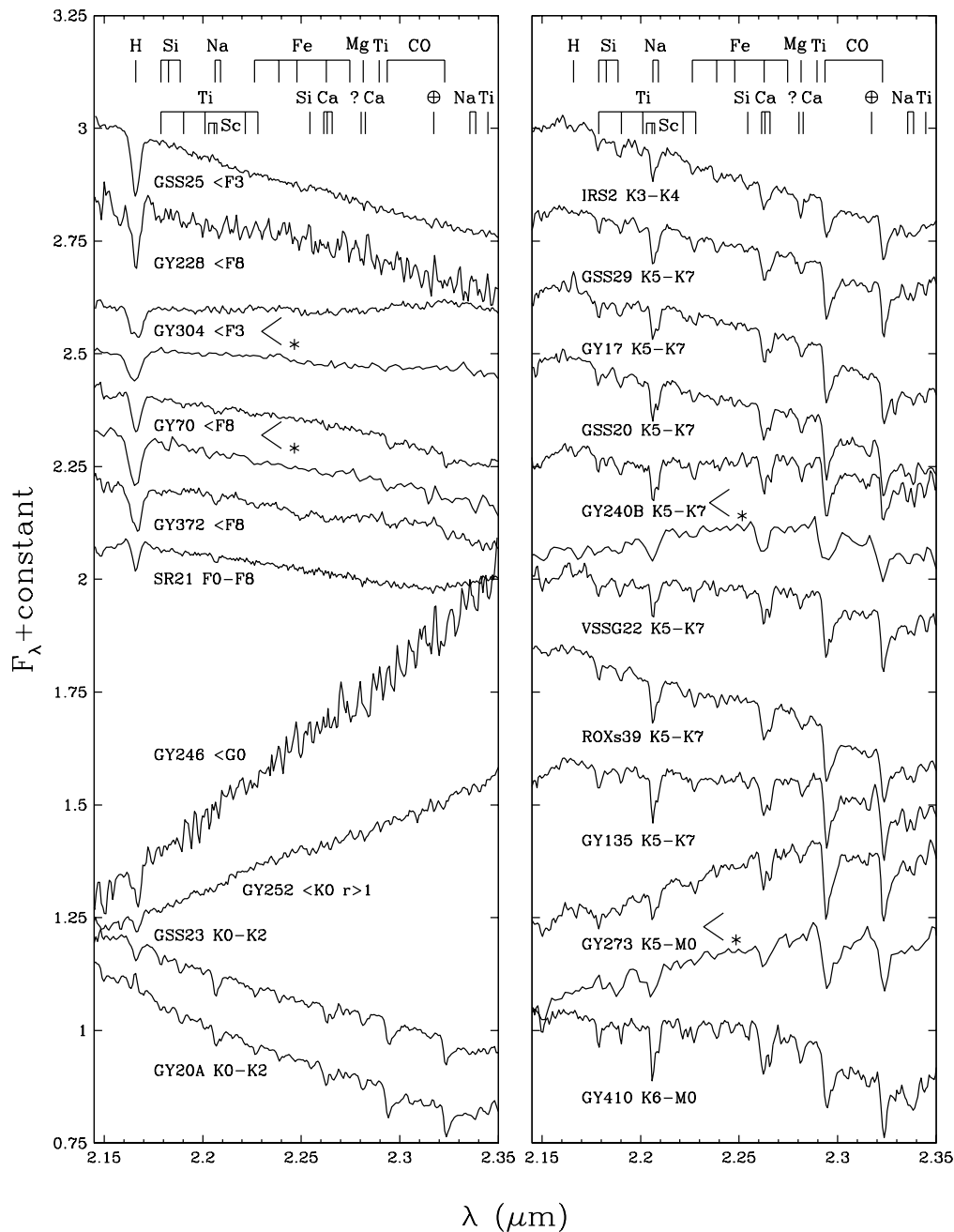
FIG. 2.—K-band spectra at $R = 1200$ of early-type stars and sources exhibiting no detectable continuum veiling ($r_K < 0.25$), with additional data at $R = 800$ (*asterisks*). Spectra are normalized at 2.2 μm with constant offsets.

vious optical and IR spectral types listed in Table 1 agree well with our measurements. Exceptions include SR 20 and GY 410, which were previously classified as G0: (Bouvier & Appenzeller 1992) and M6 (Greene & Meyer 1995), while we find very good fits with K5–M2 and K6–M0, respectively. Differences between our classifications and those of WGM are discussed in the next section.

3.1.2. Spectral Classification with H_2O Absorption

In stars later than M5, the atomic absorption lines weaken and are useful only in classification of high signal-to-noise ratio spectra. To derive spectral types for faint young low-mass candidates, we must instead rely on absorption in H_2O (1.7–2.15 μm, $\gtrsim 2.3$ μm) and CO (> 2.29 μm). Because these features are broad and become stronger

with cooler temperatures, lower spectral resolution ($R < 500$) is adequate for measuring spectral types. The CO absorption bands of young stars generally appear to arise from photospheres rather than disks (Casali & Eiroa 1996; Greene & Lada 1997), and CO and steam should form in the same region of a disk; thus, we expect the measured steam absorption to be dominated by stellar photospheres.

Detectable K-band steam absorption begins in early M dwarfs, causing the stellar continuum to peak at ~ 2.25 μm and slope down to shorter and longer wavelengths. These depressions become more pronounced with later M dwarfs until M8 V (WGM). Tokunaga & Kobayashi (1999) found that the K-band spectra of the field dwarfs vB 10 (M8 V) and DENIS-P J1058.7$-$1548 (L3 V; Kirkpatrick et al. 1999) are quite similar despite their very different optical
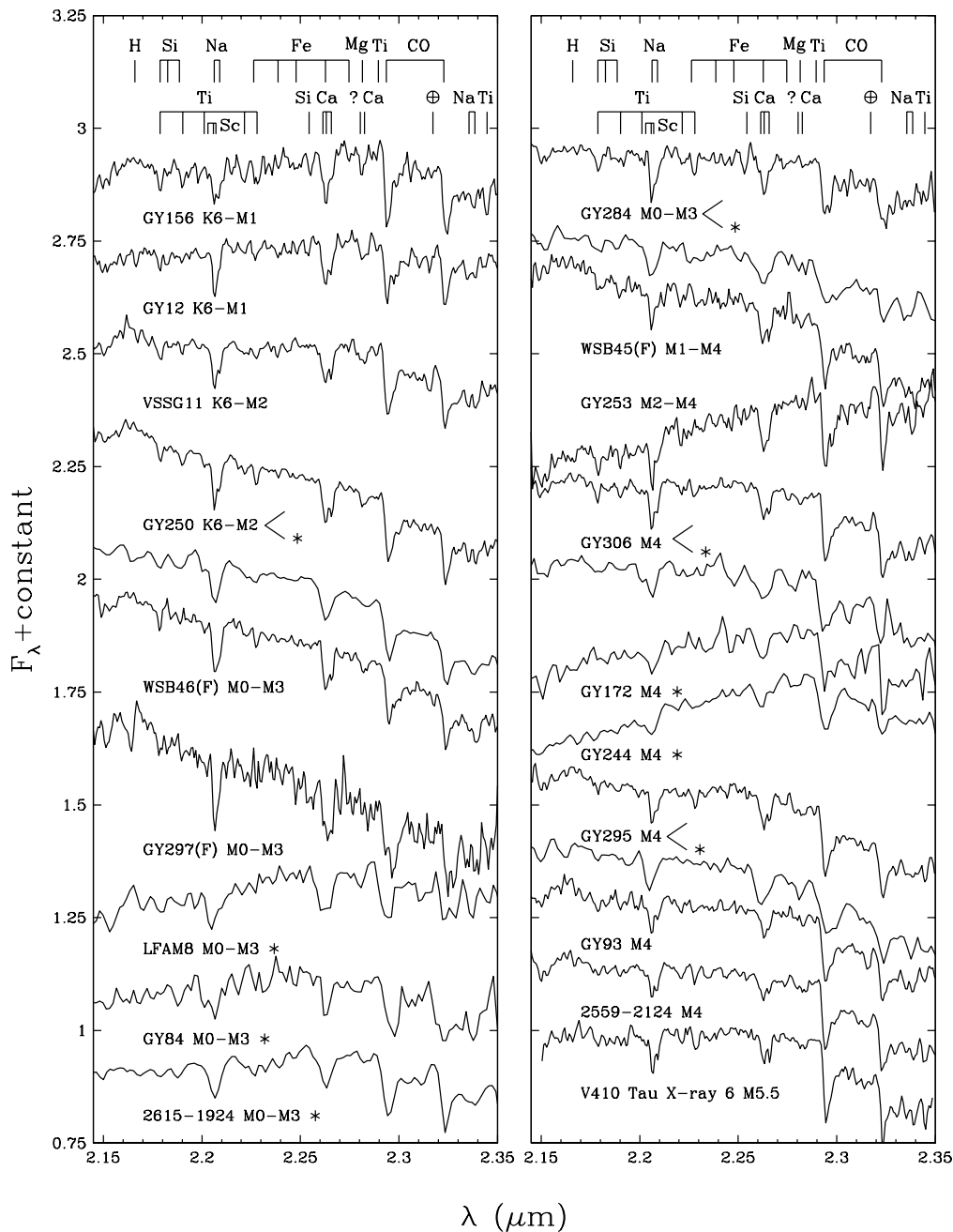
FIG. 3.—K-band spectra at $R = 1200$ of late-type sources exhibiting no detectable continuum veiling ($r_K < 0.25$), with additional data at $R = 800$ (*asterisks*). Spectra are normalized at 2.2 μm with constant offsets. Possible foreground stars ("F") are also indicated. The IR spectrum of V410 Tau X-ray 6 (LR), which is classified in the optical as M5.5 (Luhman 1999), is shown for comparison. The spectra classified as M4 are also fit marginally by veiled late-K stars with enhanced CO absorption. Spectra are normalized at 2.2 μm with constant offsets.

spectra. It is likely that the steam absorption saturates for a large range of temperatures and is thus a precise indicator of spectral type only for $< M8$ V or late L.

Steam absorption can be measured through a reddening-independent index, as demonstrated by WGM. To estimate spectral types from such an index, the stellar continuum across the entire K band must be reliably measured, requiring observations of telluric standards immediately before and after the targets and the use of the same instrument configuration for all observations. Following these guidelines in observations with FSPEC, we find that the spectral slopes are reproducible for the same object at different times, while there can be systematic differences from

instrument to instrument (e.g., FSPEC and Kitt Peak IR Cryogenic Spectrometer).

For the classification of brown dwarf candidates in ρ Oph, WGM used a relation between steam absorption and spectral type observed for M dwarfs. However, since the surface gravities of these pre–main-sequence objects are ~ 2 dex lower than those of M dwarfs, we must investigate whether steam absorption is sensitive to surface gravity over the regime from dwarfs to young stars. Thus, we have compared the K-band spectra of M dwarfs and optically classified young late-type objects. Spectra covering 2.0–2.4 μm are provided in LR for the young objects V410 X-ray 3 (M6; Strom & Strom 1994; Luhman et al. 1998a), V410
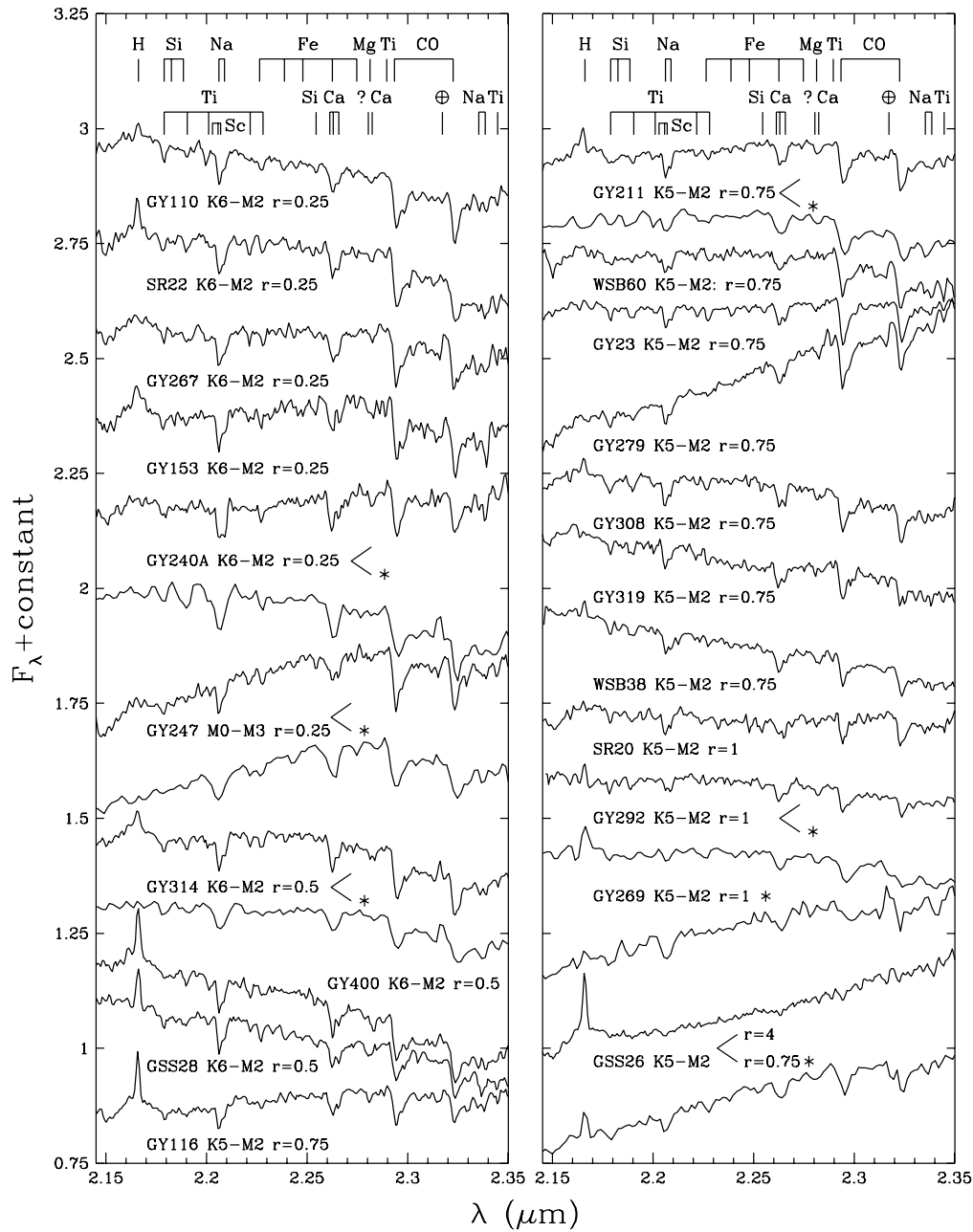
Fig. 4.—K-band spectra at $R = 1200$ of moderately veiled sources ($0.25 \leq r_K \leq 1$), with additional data at $R = 800$ (*asterisks*). Spectra are normalized at 2.2 μm with constant offsets.

X-ray 5a (M5–M5.5; Strom & Strom 1994; Briceño et al. 1998), and V410 X-ray 6 (M5; Strom & Strom 1994; M5.5, Luhman 1999). When comparing these data to a spectrum of GL 406 (M6 V; the same star used to classify Vx3 in the optical by Luhman et al. 1998a), we find that the steam in the young sources is stronger than in the dwarf counterparts. Therefore, whereas steam in dwarfs probably saturates near M8 V, saturation may begin at M6 or M7 in young sources. The deep steam absorption present in young objects may seem contrary to the weak absorption observed at the very low surface gravities ($\log g = 0$–1) of cool giants (Kleinmann & Hall 1986). However, the synthetic spectra of Allard & Hauschildt (1995) do predict the strengthening of steam that we observe from M dwarfs ($\log g \sim 5.5$) to pre–main-sequence objects ($\log g \sim 3.5$).

Using a steam absorption spectral sequence derived for evolved M dwarfs, the steam indices would imply spectral types of M6 for Vx5a and M7–M8 for Vx3 and Vx6, which are 1–2 subclasses later than their optical spectral types. To derive consistent spectral types from the steam absorption, the spectral sequence needs to be based on optically classified young stars. With Vx3, Vx5a, and Vx6 as spectral standards, we measured spectral types from the data of Williams et al. (1995) (GY 5, GY 10, GY 37, GY 202, and 162618 − 242611) and for the coolest objects in our new sample (GY 29 and GY 59). As seen in Table 1, these spectral types are systematically earlier than those reported by WGM. Note that the M6–M7 spectral types may be upper limits because of the onset of saturation in steam. We classified an additional star in the WGM sample, GY 84, with the
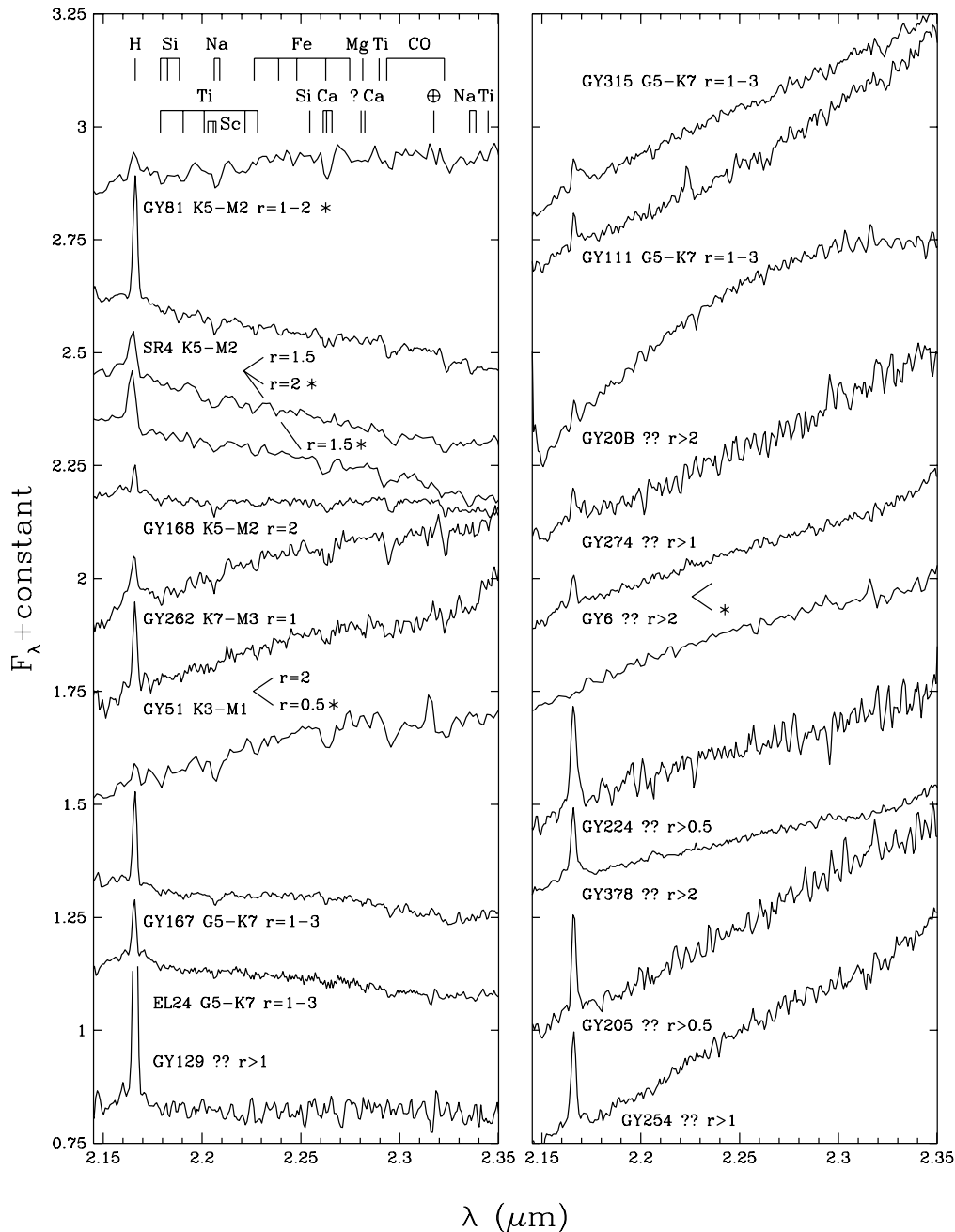
FIG. 5.—K-band spectra at $R = 1200$ of heavily veiled sources ($r_K \geq 1$) with additional data at $R = 800$ (*asterisks*). The curvature in the spectrum of GY 20B is not real and is due to difficulties in extracting the spectrum separately from the companion GY 20A. Spectra are normalized at 2.2 μm with constant offsets.

atomic absorption lines in the manner discussed in the previous section and used by LR and LRLL. We find a spectral type of early M for this object, in contrast to the M6 classification of WGM.

With the later WGM spectral types, some of the sources are very cool yet luminous and fall high above the youngest theoretical isochrones. This placement appears to be inconsistent with photometric modeling (CRCTL). These sources are moved to the left on the H-R diagram with our classifications and have more plausible temperatures given their luminosities and likely ages. The revised parameters are more consistent with the photometry of CRCTL.

The above analysis implies that the WGM spectral types are too cool by ~ 1 subclass for M6–M7 and ~ 1–2 sub-

classes for $\geq$ M8. For WGM sources that were not in our sample or could not be classified in our data, we have revised the WGM spectral types accordingly, with the results of CRCTL as an added constraint. For $162618-242416$, we adopt M5 as the spectral type, which is consistent with the data of both CRCTL and WGM. Given the apparent systematic error in WGM spectral types, the WGM classification of M8 for GY 64 is revised to M7, which agrees with CRCTL. As noted by WGM, the JHK photometry of GY 11 indicates heavy continuum veiling, which would lead to an overestimate of the temperature when steam is used in the classification. Therefore, the WGM spectral type of M6.5 probably does not need to be adjusted to an earlier type, as suggested by the temperature
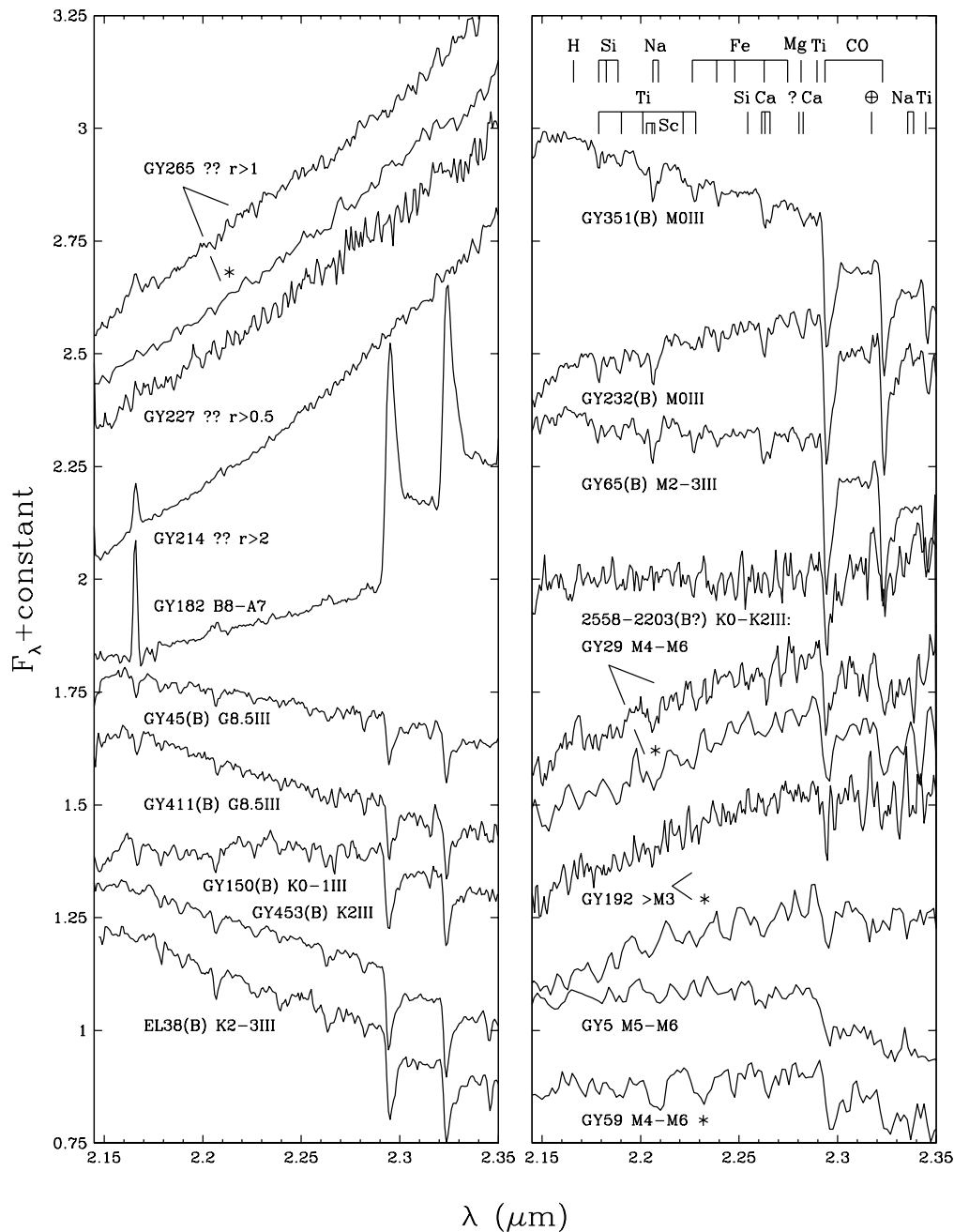
FIG. 6.—K-band spectra at $R = 1200$ of heavily veiled sources ($r_K \geq 1$), background giants ("B"), and objects with uncertain late-type classifications, with additional data at $R = 800$ (*asterisks*). Spectra are normalized at 2.2 μm with constant offsets.

estimated by CRCTL, which is equivalent to M7.5. Finally, three sources do not fall in our classified sample or the data of CRCTL. The relatively early WGM spectral types of GY 31 (M5.5) and GY 326 (M4) are adopted while the M8.5 spectral type of GY 310 is revised to M7 for use in our analysis.

3.1.3. A Possible FU Ori Object

On the northeast outskirts of the cloud, the bright IR source known as IRAS 64A (Wilking et al. 1989; Greene et al. 1994) does not appear to be a typical pre–main-sequence star. The K-band spectrum exhibits weak atomic lines and strong CO, indicative of a K giant. However, the near- and mid-IR excess emission toward this source implies youth and cluster membership. As discussed in more detail in the

Appendix, we find that the data matches that of FU Ori objects (Hartmann & Kenyon 1996). However, this object may also be a background source, such as a post-AGB star or Mira variable.

3.2. Extinction

The recent survey by BKLT provides a homogeneous set of coordinates and JHK photometry for virtually the entire spectroscopic sample (see Table 1). The photometry is in the simultaneous quad infrared imaging device (SQIID) photometric system, which is similar to CIT (Kenyon, Lada, & Barsony 1998b). Photometry and coordinates for ROXs 39 and SR 22 are taken from Greene et al. (1994, and references therein). The measurements of these two stars were converted to CIT using transformations from Humphreys,

TABLE 1

DATA FOR SPECTROSCOPIC SAMPLE IN ρ OPHIUCHI

BKLT[a]	Other ID[b]	α(1950)	δ(1950)	Previous[c]	IR	Adopt[d]	T_{eff} (K)	A_J	L_{bol} ($L_\odot$)	$J-H$	$H-K$	K	r_K[e]	$Br\gamma$ (Å)
...	SR 22	22 22.7	22 55.0	K7-M0(GM), M0(CK), M3.5(M)	K6-M2	M0	3850	0.6	0.76	0.93	0.45	8.70	0.25	1.9 ± 0.4
162536−241544......	IRS 2	22 35.59	08 57.6	K7(GM)	K3-K4	K3.5	4660	1.9	2.1	1.39	0.70	8.36	0	0
162556−242050......	SR 4, EL 13, YLW 25, IRS 12, ROXs 6, WSB 25, DoAr 20	22 54.82	14 04.5	K6(BA), K7(CK)	K5-M2	K8	3955	0.5	1.9	1.06	0.72	7.25	1.5, 2, 1.5	6.7 ± 0.3, 4.5 ± 0.5, 5.5 ± 0.5
162557−243032......	GSS 20, IRS 13, ROXs 7	22 56.11	23 46.6	K7(GM), K7(BA)	K5-K7	K6	4205	0.9	1.1	1.12	0.63	8.37	0	0
162558−242203......	...	22 57.23	15 17.7	...	K0-K2 III:	b?	...	...	...	2.57	1.46	11.41	?	0
162559−242124......	...	22 58.32	14 38.3	...	M4	M4	3180	0.0	0.21	0.65	0.45	9.52	0	0
162601−242521......	...	23 00.01	18 36.2	...	K-M:	...	...	...	...	1.90	1.23	11.10	?	0
162603−242337......	GSS 23, DoAr 21, EL 14, ROXs 8, VSS 93	23 01.65	16 52.4	K0(BA), K0(M)	K0-K2	K1	5080	1.6	18	1.26	0.59	6.16	0	0
162605−242451(c) ...	...	23 03.64	18 05.9	Early(WGM)	...	b	...	...	...	>1.1	1.91	13.99	...	...
162609−243411......	...	23 07.84	27 26.6	A0(SR)	<F3	A0	9520	2.3	160	0.86	0.49	6.42	0	0
162610−242056......	GSS 25, VSS 92, EL 16, YLW 28, SR 3	23 08.97	14 11.6		K5-M2	K8	3955	6.0	1.3	3.34	2.25	9.38	4, 0.75	2.9 ± 0.2, 1.7 ± 0.3
162615−241924(c) ...	GSS 26	23 14.49	12 40.0		M0-M3	M1.5	3595	4.6	0.80	2.51	1.46	9.98	0	0
162616−242225(c) ...	GSS 29, EL 18	23 15.46	15 40.7	K7-M0(GM)	K5-K7	K6	4205	3.0	3.1	1.88	1.04	8.19	0	...
162617−242023(c) ...	GSS 28, DoAr 24, EL 19, ROXs 10A, WSB 27	23 15.71	13 39.3	K7-M0(GM), K5(BA)	K6-M2	M0	3850	0.8	1.2	1.05	0.58	8.09	0.5	1.9 ± 0.15
162618−242818......	...	23 16.61	21 33.6	Early(WGM)	...	b	...	...	...	2.57	1.43	12.93	...	...
162618−242611(c) ...	...	23 17.54	19 27.4	M7.5(WGM)	M5-M6[f]	M5.5	2925	3.1	0.050	1.75	1.20	12.18	...	...
162618−242616(c) ...	...	23 17.56	17 32.2	M5(WGM)	K-M	M5	3010	5.0	0.097	2.46	1.95	11.94	0	...
162621−243306(c) ...	GY 6, GSS 30, EL 21	23 19.99	16 22.1		?	...	...	...	...	3.06	2.51	8.32	> 2	2.0 ± 0.2, <0.5
162621−242602(c) ...	GY 5	23 20.27	19 17.7	M7(WGM)	M5-M6[f]	M5.5	2925	1.4	0.11	1.13	0.66	10.91	<1	...
162622−243354(c) ...	GY 10	23 20.78	17 10.2	M8.5(WGM)	M6-M7[f]	M6.5	2780	4.0	0.067	2.16	1.34	12.25	...	...
162622−242409(c) ...	GY 11	23 20.89	17 25.1	M6.5(WGM)	...	M6.5	2780	1.4	0.0028	1.15	1.22	14.15	...	...
162622−242254(c) ...	GY 12	23 20.99	16 10.8	M2(GM)	K6-M1	K8	3955	4.6	0.68	2.75	1.87	9.60	0	0
162623−242101(c)[g] ...	GY 20A, DoAr 24E, GSS 31, EL 22, ROXs 10B, WSB 30	23 22.01	14 17.6	K0(BA)	K0-K2	K1	5080	1.8	10	1.52	0.93	6.44	0	0.7 ± 0.2
162623−242101(c)[g] ...	GY 20B, DoAr 24EB	23 22.01	14 17.6	...	?	...	...	...	...	...	...	...	> 2	1.5 ± 0.4
162623−244311......	GY 17, DoAr 25	23 22.04	36 27.7	K4(GM), K7(M)	K5-K7	K6	4205	0.0	1.0	0.93	0.79	7.57	0	0.9 ± 0.2
162623−242441(c) ...	GY 21, LFAM 3	23 22.14	17 57.4	K-M(GM), M0(GL)	K-M:	M0	3850	3.8	0.36	2.45	1.69	9.94	1(GL)	2.0 ± 0.7
162624−242449(c) ...	GY 23, S2, GSS 32, EL 23	23 22.64	18 05.6	K(GM)	K5-M2	K8	3955	3.1	3.9	2.15	1.48	7.20	0.75	0
162624−241616......	EL 24, YLW 32	23 22.85	09 32.0	...	G5-K7	...	...	2.3	...	1.95	1.46	6.77	1-3	2.7 ± 0.2
162625−242325(c) ...	GY 31	23 23.86	16 41.7	M5.5(WGM)	...	M5.5	2925	16	1.0	...	3.98	13.09	...	...
162625−242446(c) ...	GY 29	23 23.87	18 02.7	M6(WGM)	M4-M6	M5	3010	6.3	0.47	2.95	2.11	10.86	0	0
162627−242643(c) ...	GY 37, VSSG 29	23 26.38	19 59.5	...	M6[f]	M6	2840	1.8	0.037	1.31	0.95	11.99	...	...
162629−241908......	LFAM 8	23 28.31	12 24.3	...	M0-M3	M1.5	3595	6.6	0.46	3.37	2.05	11.19	0	0
162630−242258(c) ...	GY 45	23 28.45	31 57.4	...	G8.5 III	b	...	...	...	2.40	1.36	8.31	...	...
162630−242841......	GY 51, VSSG 27	23 29.12	16 15.3	...	K3-M1	b	...	...	...	3.23	2.74	10.72	2, 0.5	5.0 ± 0.5, 1.5 ± 0.5
162631−242531(c) ...	GY 59	23 29.95	18 48.0	M6(WGM)	M4-M6	M5	3010	3.4	0.099	1.86	1.21	11.68	...	...
162632−242636(c) ...	GY 64	23 31.11	19 53.4	M8(WGM)	M4-M6	M7	2720	3.2	0.014	1.87	1.43	13.33	...	...
162633−243625......	GY 65	23 31.34	29 42.4	...	M2-3 III	b	...	...	...	2.58	1.49	8.91	0	0
162634−242330(c) ...	GY 70, S1, GSS 35, VSS 26, EL 25, ROXs 14, YLW 36	23 32.78	16 47.1	B2-B5(BA, GSS, CK)	<F8	B3	18700	...	...	1.56	0.96	6.32	0	0
162637−242302......	GY 81, VSSG 4	23 36.42	16 19.4	...	K5-M2	K8	3955	4.6	0.20	2.79	1.91	10.92	1-2	3.0 ± 0.5
162638−242324......	GY 84	23 37.43	16 41.6	M6(WGM)	M0-M3	M1.5	3595	4.6	0.24	2.40	1.26	11.63	0	0
162641−244015......	GY 93, WSB 37	23 39.72	33 33.0	K-M(GM)	M4	M4	3180	0.6	0.31	0.98	0.55	9.20	0	0

TABLE 1—Continued

BKLT[a]	Other ID[b]	α(1950)	δ(1950)	Previous[c]	IR	Adopt[d]	T_{eff} (K)	A_J	L_{bol} ($L_\odot$)	J − H	H − K	K	r_K[e]	Brγ (Å)
162642−242224	GY 107	23 41.32	15 42.0	M3?(WGM)	...	b	...	...	...	2.02	0.97	11.40	...	...
162642−242031	GY 110, VSSG 2, EL 26, GSS 37	23 41.48	13 49.0	M0(GM), K6(M)	K6−M2	M0	3850	2.9	3.5	1.78	0.93	8.00	0.25	0.6 ± 0.2
162643−241635	VSSG 11, IRS 19	23 42.42	09 52.9	M3(GM)	K6−M2	M0	3850	4.0	1.1	2.27	1.27	9.58	0	0
162644−243447	GY 111, WL 12, YLW 2, VSSG 30	23 42.66	28 04.7	...	G5−K7	...	...	...	...	3.79	2.89	10.18	1−3	1.8 ± 0.4
162645−242309	GY 116, GSS 39, EL 27, VSSG 28	23 43.62	16 26.9	M(GM)	K5−M2	K8	3955	4.7	2.1	2.64	1.62	8.88	0.75	2.1 ± 0.15
162646−241203	WSB 38, VSS 27, ROXs 16	23 45.16	05 20.9	K(GM), G9:(BA)	K5−M2	K8	3955	1.9	3.4	1.47	0.82	7.51	0.75	0.6 ± 0.15
162648−242840(c)	GY 128, WL 2	23 47.05	21 57.9	K−M(GM)	K−M:	...	...	...	...	>2.95	3.06	10.99	?	0
162649−243823	GY 129, WL 18	23 47.47	31 41.3	...	?	?	...	2.6	...	1.99	1.39	9.82	>1	13.7 ± 0.5
162649−242005	GY 135, VSSG 3, LFAM 18	23 47.86	13 23.0	K7−M0(GM)	K5−K7	K6	4205	4.4	4.4	2.33	1.20	8.62	0	0
162651−243242(c)	GY 141	23 49.82	26 00.4	M8.5(LLR)	K0−1 III	M8.5	2500	0[h]	0.0026[h]	0.76	0.50	13.87	...	0
162653−242229	GY 150, GSS 40, VSSG 6, IRS 21	23 52.47	15 47.6	...	K6−M2	b	...	...	...	2.86	1.67	9.85	0.25	0
162654−242622	GY 153, VSSG 5	23 53.04	19 40.2	M2(GM)	K6−M2	M0	3850	5.8	1.2	3.02	1.82	9.88	0	1.7 ± 0.4
162654−242231	GY 156, VSSG 6, GSS 40	23 53.58	15 49.4	...	K6−M1	K8	3955	6.1	1.3	3.07	1.78	10.19	...	0
162656−242838(c)	GY 163	23 55.47	21 56.8	M2.5(WGM)	...	M2.5	3430	9.0	0.26	>2.06	2.28	12.66	...	...
162658−244529	GY 168, SR 24N, IRS 24, EL 28	23 56.58	38 48.1	K2(GM), M0.5(CK), M0(M)	K5−M2	K8	3955	2.0	2.3	1.70	1.18	7.42	2	1.3 ± 0.2
162658−244534	GY 167, SR 24S, IRS 25, EL 28	23 56.64	38 52.9	K2(GM), K2:(CK), K7(M)	G5−K7	K2	4900	1.2	2.4	1.50	1.17	7.08	1−3	4.7 ± 0.15
162659−243556(c)	GY 172, WL 14	23 57.42	29 14.7	...	M4	M4	3180	5.1	0.14	2.74	1.64	11.74	0	0
162702−243726(c)	GY 182, WL 16	24 00.64	30 45.0	...	B8−A7[i]	...	...	...	...	3.56	2.66	7.92	?	7.2 ± 0.2
162704−242830(c)	GY 192, WL 1, YLW 6, IRS 29, VSSG 31	24 02.61	21 49.3	...	>M3	...	...	...	...	3.15	2.26	10.81	?	0
162706−242837(c)	GY 202	24 04.47	21 56.0	M7(WGM)	M6−M7[f]	M6.5	2780	3.9	0.022	2.09	1.70	12.97	...	...
162706−243814(c)	GY 205, WL 17	24 05.06	31 33.3	...	?	?	...	...	...	3.33	3.29	10.28	>0.5	5.9 ± 0.4
162709−243408(c)	GY 211, WL 10	24 07.48	27 27.0	...	K5−M2	K8	3955	3.6	1.4	2.22	1.39	8.85	0.75	1.4 ± 0.2, <0.8
162709−243718(c)	GY 214, EL 29, WL 15, YLW 7	24 07.71	30 37.4	...	?	...	...	...	...	5.20	4.47	7.54	>2	3.0 ± 0.1
162710−241914	SR 21, VSSG 23, VSS 31, EL 30, YLW 8	24 08.78	12 33.7	G1(M)	F0−F8	F4	6590	2.7	51	1.23	1.03	6.30	<1	8.5 ± 1.0
162711−244046	GY 224	24 09.38	34 05.7	...	?	...	...	...	...	>3.31	2.90	10.79	>0.5	0
162711−243832(c)	GY 227, WL 19	24 10.00	31 51.2	...	?	...	...	...	...	...	>4.27	11.23	>0.5	0
162711−242343	GY 228, IRS 32	24 10.25	17 02.6	...	<F8	...	...	...	...	2.63	1.58	10.06	?	0
162712−243449(c)	...	24 10.49	28 08.4	...	K−M:	...	...	...	...	2.37	1.76	11.53	?	0
162713−244133	GY 232	24 11.44	34 52.5	...	M0 III	...	...	...	...	>4.46	2.96	9.58	...	0
162714−245132	WSB 45, ROXs 20A	24 12.34	44 51.7	M5(BA)	M1−M4	PMS?, dMe?	...	...	...	0.79	0.34	10.39	0	0
162715−245137	WSB 46, ROXs 20B	24 12.98	44 57.2	M2(BA)	M0−M3	PMS?, dMe?	...	...	...	0.90	0.46	9.51	0	0
162715−242640(c)	GY 239, IRS 34, YLW 10B	24 13.99	19 59.9	K(GM)	K−M:	M0	3850	4.9	1.4	>3.53	2.81	10.66	?	0
162715−243843(c)[g]	GY 240A, WL 20	24 14.08	32 02.9	K7−M0(GM)	K6−M2	M0	3850	4.9	0.55	2.67	1.57	9.21	0.25	0
162715−243843(c)[g]	GY 240B, WL 20	24 14.08	32 02.9	K−M(GM)	K5−K7	K6	4205	...	...	2.67	1.57	9.21	0	0
162717−242856(c)	GY 244, YLW 12A, IRS 37, VSSG 26	24 16.06	22 16.1	...	M4	M4	...	~11[j]	...	>3.1	2.95	10.95	?	0
162718−242853(c)	GY 246, WL 5, VSSG 26, IRS 38	24 16.65	22 12.6	F7(GM)	<G0	...	...	...	...	>2.68	4.04	10.28	?	0
162718−242906(c)	GY 247, WL 4, IRS 39, VSSG 26	24 16.95	22 25.6	M(GM)	M0−M3	M1.5	3595	5.4	1.6	3.00	1.93	9.13	0.25	0
162719−244139(c)	GY 250, SR 12, IRS 40, ROXs 21, YLW 13A	24 17.67	34 59.5	K4/M2.5(BA), M1(CK)	K6−M2	M0	3850	0.2	0.66	0.73	0.28	8.41	0	0
162721−244142(c)	GY 252, YLW 13B, IRS 42	24 19.63	35 02.5	...	<K0	...	...	...	...	3.90	2.90	8.41	>1	0
162721−244335	GY 253	24 19.95	36 55.5	...	M2−M4	M3	3350	8.2	0.83	4.03	2.53	10.78	?	0
162721−242953(c)	GY 254, YLW 14, WL 6	24 20.26	23 12.9	...	?	...	...	...	...	>2.61	4.35	10.04	>1	6.2 ± 0.4
162722−241759	VSSG 22	24 21.51	11 19.1	K7−M0(GM)	K5−K7	K6	4205	4.6	1.8	2.48	1.38	9.41	0	0

TABLE 1—*Continued*

BKLT[a]	Other ID[b]	α(1950)	δ(1950)	Previous[c]	IR	Adopt[d]	T_{eff} (K)	A_J	L_{bol} ($L_\odot$)	$J-H$	$H-K$	K	r_K[e]	Brγ (Å)
162726−243923(c)...	GY 262	24 24.67	32 44.0	...	K7−M3	M1	3680	6.4	1.0	3.46	2.30	9.77	1	2.2 ± 0.3
162726−244051(c)...	GY 265, YLW 15A, IRS 43	24 25.09	34 11.6	...	?	...	...	...	...	>3.83	3.71	9.46	>1	1.5 ± 0.7, <0.5
162727−243116...	GY 267, VSSG 25, EL 31, WL 13	24 25.83	24 37.0	K−M(GM)	K6−M2	M0	3850	3.1	0.92	1.93	1.11	9.30	0.25	0
162728−243934...	GY 269, YLW 16A, IRS 44	24 26.22	32 54.5	...	K5−M2	K8	...	...	...	>3.91	3.44	9.65	1	0
162728−242721...	GY 273, VSSG 18, EL 32, IRS 45	24 26.92	20 42.1	...	K5−M0	K6.5	4132	5.0	0.86	2.99	2.09	9.39	1	0
162729−243917...	GY 274, YLW 16B, IRS 46	24 27.63	32 37.2	...	?	...	...	...	...	>2.35	3.19	11.46	>1	2.0 ± 0.6
162730−242744...	GY 279, VSSG 17, EL 33, IRS 47	24 28.65	21 04.6	M(GM), ≥M2(GL)	K5−M2	K8	3955	6.9	1.8	3.80	2.69	8.95	0.75, 1(GL)	0
162730−242457...	GY 284	24 29.37	18 17.4	...	M0−M3	M1.5	3595	2.4	0.35	1.69	0.97	10.04	0	0
162733−244115(c)...	GY 292	24 31.29	34 36.2	...	K5−M2	K8	3955	2.9	2.1	2.04	1.37	7.92	1	1.0 ± 0.4, 3.0 ± 1
162735−243834...	GY 295	24 33.50	31 55.0	...	M4	M4	3180	1.3	0.36	1.13	0.51	9.64	0	0
162736−242833...	GY 297	24 34.95	21 54.7	...	M0−M3	f	...	...	...	0.68	0.25	11.04	0	0
162737−243035...	GY 304, YLW 46A, IRS 48	24 35.63	23 56.0	...	<F3	...	...	...	...	1.88	1.23	7.42	?	0
162738−243043...	GY 306, IRS 50	24 36.57	24 03.9	...	M4	M4	3180	3.1	0.63	1.87	1.01	9.59	0	0
162738−243658...	GY 308, IRS 49	24 36.67	30 19.1	...	K5−M2	K8	3955	2.9	1.7	1.96	1.24	8.31	0.75	0.8 ± 0.2, <2
162738−243838...	GY 310	24 36.90	31 59.1	M8.5(WGM)	...	M7	2720	1.7	0.079	1.29	0.83	11.08	...	...
162739−243914...	GY 314	24 37.68	32 35.6	M(GM)	K6−M2	M0	3850	2.0	1.4	1.55	0.92	8.35	0.5	1.6 ± 0.3, <0.5
162739−244316...	GY 315, YLW 45, IRS 51	24 37.97	36 37.0	...	G5−K7	...	...	~9.5	...	4.70	3.49	8.93	1−3	2.0 ± 0.6
162740−242205...	GY 319, SR 9, EL 34, ROXs 29, IRS 52, DoAr 34, WSB 54	24 38.83	15 26.4	K4(GM), K7(CK), K4/K6(BA)	K5−M2	K8	3955	0.0	2.0	0.77	0.51	7.20	0.75	0
162742−243849...	GY 326	24 40.96	32 10.9	M4(WGM)	M4	M4	3180	3.2	0.36	1.78	0.88	10.59	...	...
162746−242323...	GY 351, VSSG 13, EL 35	24 45.25	16 45.2	...	M0 III	b	...	...	...	2.20	1.12	7.29	...	0
162749−242540...	GY 372, VSSG 14, EL 36	24 48.37	19 02.5	A7(GM), A7:(M)	<F8	...	...	...	...	1.20	0.82	7.32	0	0
162751−243145...	GY 378, YLW 52, IRS 54	24 50.26	25 07.6	...	?	...	...	...	...	3.13	2.63	10.87	>2	4.3 ± 0.4
162755−242619...	GY 400, SR 10	24 53.97	19 41.0	M1.5(CK)	K6−M2	M0	3850	0.0	0.55	0.50	0.60	8.74	0.5	2.5 ± 0.3
162757−244004...	GY 410	24 56.08	33 26.1	M6(GM)	K6−M0	K7	4060	2.7	0.64	1.72	0.92	9.78	0	0
162757−243751...	GY 411	24 56.19	31 13.3	...	G8.5 III	b	...	...	...	2.20	1.21	9.52	...	0
162803−242632...	GY 453, VSSG 16, EL 37, IRS 58	25 02.13	19 55.5	...	K2 III	b	...	...	...	1.10	0.77	6.89	...	0
162809−242322...	EL 38, VSSG 15	25 07.71	16 45.0	...	K2−3 III	b	...	...	...	1.52	0.82	7.12	...	0
162816−243657...	WSB 60, YLW 58	25 14.88	30 20.9	K−M(GM)	K5−M2:	K8	3955	0.7	0.28	1.16	0.78	9.43	0.75	0
162823−242241...	SR 20, ROXs 33, DoAr 38, WSB 61	25 21.82	16 05.7	G0:(BA)	K5−M2	K8	3955	2.1	0.93	1.69	1.13	8.55	1	0
162923−241359...	IRAS 64A	26 22.00	07 27.1	...	?[k]	...	...	...	...	1.79	0.91	6.45	?	0
....	ROXs 39	27 33.8	27 51.0	K5(BA)	K5−K7	K6	4205	0.0	1.4	0.66	0.27	8.00	0	0

NOTES.—*JHK* photometry and coordinates are taken from BKLT. The data for ROXs 39 and SR 22 are from Greene et al. 1994, and references therein. Photometry for GY 31 is from Comeron et al. 1993. Units of right ascension (prefixed by 16[h]) are minutes and seconds, and units of declination (prefixed by −24°) are arcminutes and arcseconds.

[a] Sources falling within the cloud core as defined in Fig. 1 are indicated by "(c)."

[b] SR = Struve & Rudkjøbing 1949, DoAr = Dolidze & Arakelyan 1959, S and GSS = Grasdalen, Strom, & Strom 1973, VSSG = Vrba et al. 1975, VSS = Vrba, Strom, & Strom 1976, EL = Elias 1978, ROX = Montmerle et al. 1983, WL = Wilking & Lada 1983, YLW = Young et al. 1986, WSB = Wilking, Schwartz, & Blackwell 1987, IRAS = Table 2 of Wilking et al. 1989, IRS = Table 1 of Wilking et al. 1989, LFAM = Leous et al. 1991, GY = Greene & Young 1992.

[c] IR spectral types of Greene & Meyer 1995, Greene & Lada 1997, and Wilking et al. 1998. Optical spectral types of Struve & Rudkjøbing 1949, Grasdalen et al. 1973, Cohen & Kuhi 1979, Bouvier & Appenzeller 1992, Luhman et al. 1997, and Martin et al. 1998.

[d] Background and foreground stars are indicated by "b" and "f."

[e] Derived from the IR spectra in this work.

[f] Data from Williams et al. 1995 used in classification.

[g] GY 20 and GY 240 are each binary systems that appear as one source in the coordinates and photometry of BKLT.

[h] Luhman et al. 1997.

[i] *H*-band classification by Biscaya et al. 1999.

[j] Extinction was derived by assuming that $H - K$ is not affected significantly by excess emission, as suggested by the $r_K \sim 0$ measured in the spectrum.

[k] The optical spectral type is M8–M9 III, while the IR spectrum exhibits CO absorption equivalent to K4 III and is very similar to spectra of FU Ori objects.

Jones, & Sitko (1984) and Leggett (1992). Since the ρ Oph cloud core represents a relatively small fraction of the square degree observed by BKLT, most of their survey region has low reddening and background stars are likely to dominate the stellar counts. Under this assumption, Kenyon et al. (1998b) used the IR color-color diagram to measure an extinction slope of $E(J-H)/(H-K) = 1.57 \pm 0.03$. We have spectroscopically identified several background stars, whose colors in Figure 7 are consistent with this reddening vector. For dereddening individual sources, we used the extinction law of Rieke & Lebofsky (1985). Although it differs from the slope found by BKLT, the difference is minor and the slope of BKLT alone cannot be interpreted in terms of individual color reddening coefficients.

Figure 7 shows $H-K$ versus $J-H$ diagrams where the main sequence and the locus of classical T Tauri stars (CTTS) (Meyer, Calvet, & Hillenbrand 1997) are plotted

with their respective reddening bands. In the first three panels we present the spectroscopic sample as a function of r_K. The sources behave as expected. Those with heavily veiled spectra and large $H-K$ excesses fall on the reddened CTTS locus or to the right of it. Moderately veiled objects tend to fall between the reddened main sequence and the extension provided by the CTTS locus. Objects with no detectable veiling and normal colors are consistent with reddened main-sequence stars. This behavior is similar to the trend observed by Casali & Matthews (1992) and Casali & Eiroa (1996) in spectra of CO absorption in a smaller sample of young stars. The scatter in this correlation, where a few sources with large r_K have small excesses in $H-K$, or vice versa, can be explained by variability in the excess continuum emission (mostly at K). Such variability is evident in the data for GSS 26 and GY 51 (see § 4.4.3.)

Extinctions were estimated for stars earlier than G0 by dereddening to the main-sequence value of $J-H$ for a given
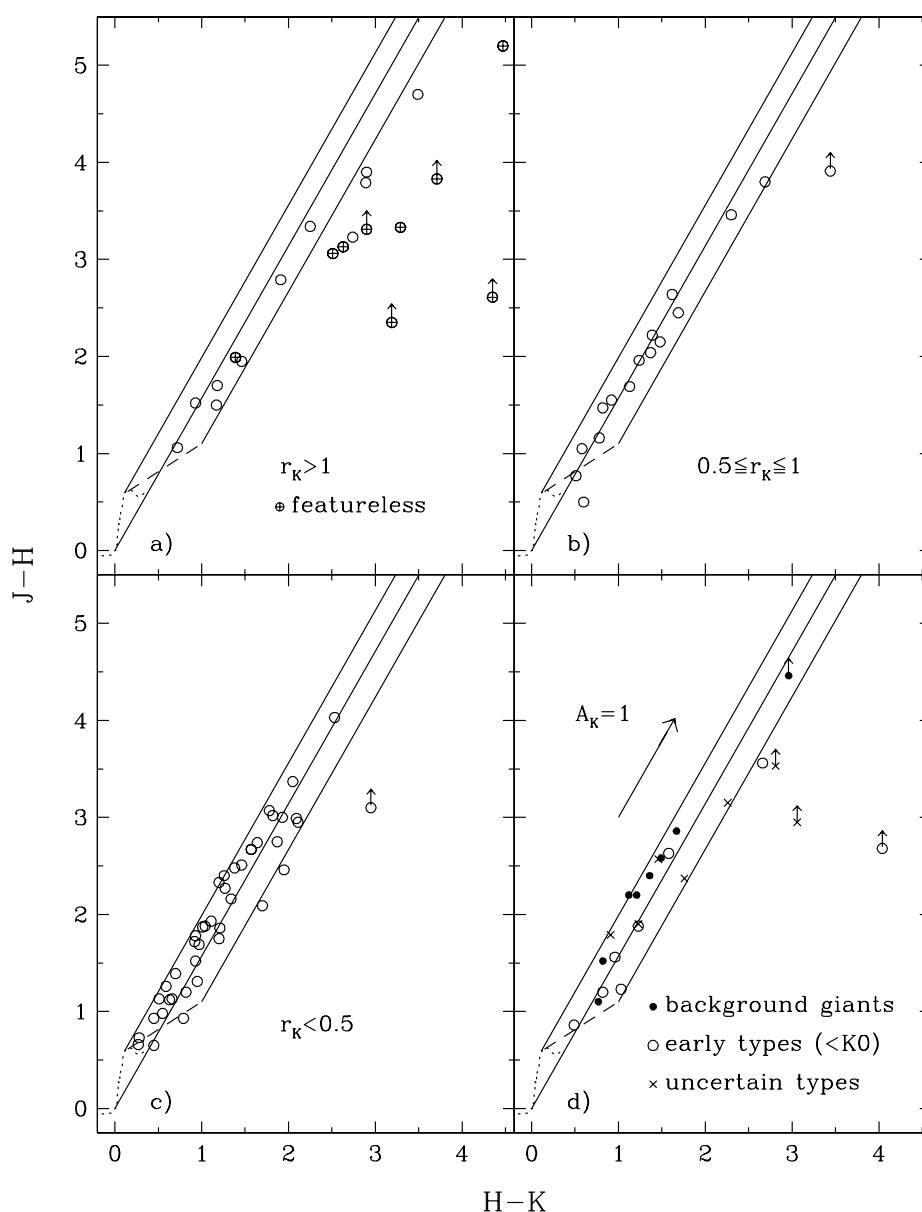
Fig. 7.—(a, b, and c) $H-K$ vs. $J-H$ for the K-band spectroscopic sample as a function of the continuum veiling, r_K, measured in the spectra. (d) Background giants, early-type stars, and sources with uncertain late-type classifications. The main sequence (dotted line) and CTTS locus (dashed line) are shown along with the reddening bands of each, where the reddening vectors were derived from BKLT data by Kenyon et al. (1998b).

spectral type. Reddenings for late-type stars are often also estimated by assuming main-sequence values for the intrinsic colors. In an older cluster such as IC 348 (0.5–10 Myr), since much of the population consists of evolved class III sources that show little evidence for disks, this approach for low-mass stars is reasonable. On the other hand, in a very young cluster such as ρ Oph (<1 Myr), many of the stars are class I through class II with IR colors affected substantially by emission from circumstellar disks and envelopes.

By using $E(R-I)$ to deredden the $J-H$ and $H-K$ colors, Meyer et al. (1997) derived a locus of intrinsic colors for CTTS in Taurus, which are equivalent to class II sources. The CTTS locus is shown as the dashed line in Figures 7 and 8 and has been reproduced by models of star-disk systems (Lada & Adams 1992; Meyer et al. 1997).

The CTTS locus of Meyer et al. (1997) was measured for stars of spectral types near M0, where the origin of the locus falls at the main-sequence colors of M0. As predicted by Meyer et al. (1997) and observed by Luhman (1999) in IC 348, the locus and its origin are shifted to redder $H-K$ for later M spectral types. For earlier stars that fall within the reddening band of the CTTS locus, extinctions were calculated by dereddening the $J-H$ and $H-K$ colors to this locus. Sources to the right of the CTTS reddening band in Figure 7 are heavily veiled and have uncertain spectral types; consequently, they are not plotted in the H-R diagram.

3.3. Effective Temperatures and Luminosities

To convert spectral types and photometry to effective temperatures and bolometric luminosities, we have adopted the temperature scale and procedures discussed in detail by LR and LRLL. We combined the dereddened J photometry with the bolometric corrections compiled by Kenyon & Hartmann (1995) and a distance modulus of 6.1 (Whittet 1974) to arrive at the bolometric luminosities. The source extinctions at J, effective temperatures, and bolometric

luminosities are listed in Table 1, where the interstellar reddening law of Rieke & Lebofsky (1985) is used with A_J in the Johnson-Glass photometric system.

No J photometry is available for two sources in our sample, GY 244 and GY 269. Since both show strong emission in the mid-IR, the $H-K$ color may be contaminated significantly by excess at K. Our measurements of r_K from the spectra could be used to correct for this effect, but since veiling can be variable and the spectra and colors were not measured simultaneously, we refrain from this approach. Although we cannot reliably place it on the H-R diagram, we will use the spectral type of GY 244 and a canonical age to arrive at an approximate mass that can be added to the IMF for the cloud core in § 4.3.1. Such an estimate was not necessary for GY 269, which falls outside of the cloud core. For the B star S1, we refer to the calorimetric luminosity derived by Wilking et al. (1989).

4. THE ρ OPH STELLAR POPULATION

4.1. Cluster Membership

Classic methods of determining cluster membership (e.g., proper motions, Li absorption) are unavailable for most of the stars in our spectroscopic sample. However, we can confidently distinguish cluster members from field contaminants—foreground and background stars—through other means. With K-band spectra of modest signal-to-noise ratio, background giants are easily identified through their distinctive continuum structure and strong CO absorption. All of the background giants in our sample appear in the less reddened area surrounding the ρ Oph cloud core, as indicated in Figure 1. The sample of WGM includes one likely background giant and two background early-type stars. GY 297 shows little or no reddening in the IR colors and has no other indications of youth or cluster membership, such as near- or mid-IR excess emission or weakening of Na expected for young M stars (Luhman et al.
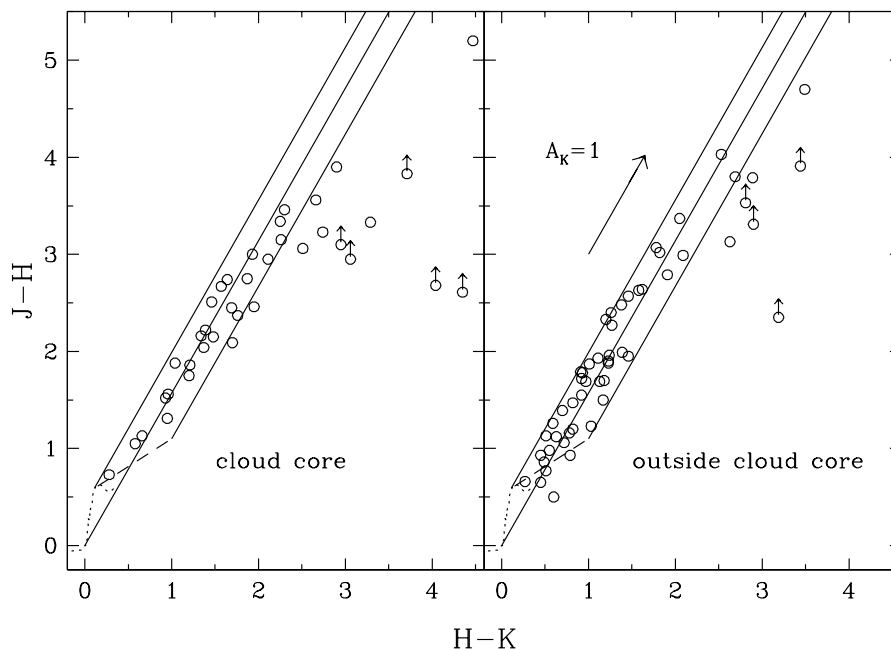

FIG. 8.—$H-K$ vs. $J-H$ for the K-band spectroscopic sample within and outside the cloud core, as defined by dashed boundary in Fig. 1. Background and foreground stars have been omitted. The main sequence (dotted line) and CTTS locus (dashed line) are shown along with the reddening bands of each, where the reddening vectors were derived from BKLT data by Kenyon et al. (1998b).

1998a, 1998b). It is a probable foreground star and is omitted from further analysis. WSB 45 and WSB 46 are a close pair (10″) and show no obvious reddening in their IR colors or Li absorption (WSB 45, Bouvier & Appenzeller 1992). Strong, variable X-ray emission and weak Hα emission (3–6 Å) have been detected toward these sources (Montmerle et al. 1983), suggesting they are either pre–main-sequence stars or active field dwarfs. We omit these stars for our discussion here. The remaining sources are unlikely to be background or foreground stars since they fall above the main sequence and have reddened colors. To examine cluster membership at fainter magnitudes beyond the limit of our spectroscopic sample, we will use a newly acquired KLF and diagrams of $H - K$ versus K to develop

a model for the background star population shining through the cloud core (§ 4.3.5).

4.2. The H-R Diagram and Star Formation History

We use the estimates of $T_{\rm eff}$ and $L_{\rm bol}$ from § 3.3 to place the K-band spectroscopic sample on H-R diagrams in Figure 9. All additional sources observed by WGM and Luhman et al. (1997) are also included. We have omitted objects with uncertain spectral types (<F8, K–M, featureless) and the foreground and background stars. The diagram of $H - K$ versus K in Figure 10 indicates that the core spectroscopic sample is complete to $K_{\rm dereddened} = 11$ for $H - K < 2$ ($A_K < 3$), corresponding to the dashed line on the H-R diagram for the core.
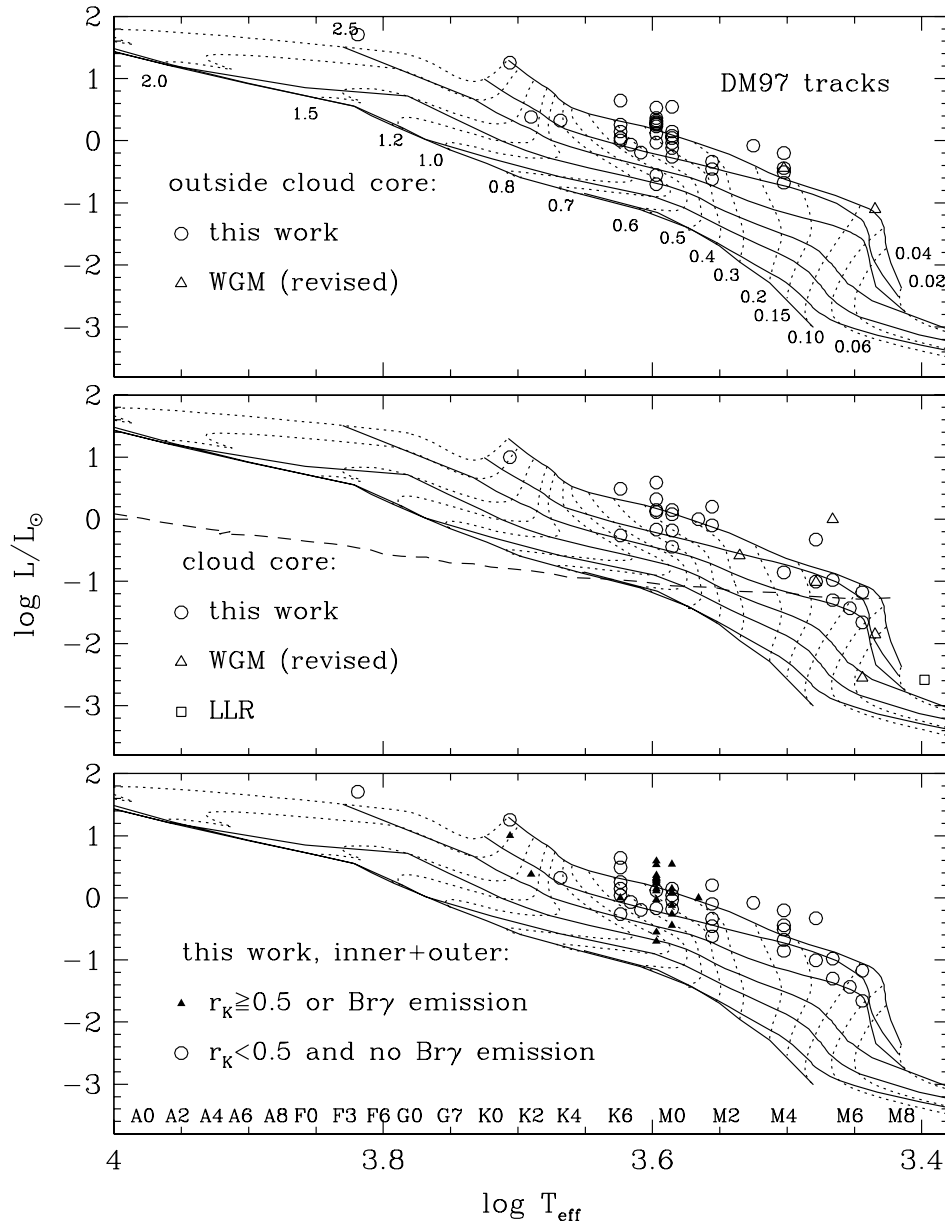
FIG. 9.—The H-R diagram of the ρ Oph star-forming region (*top panel*) outside and (*middle panel*) within the cloud core, as defined by the dashed boundary in Fig. 1. Low-mass sources observed by WGM and Luhman et al. (1997) are also shown. *Bottom panel*: Comparison of sources in our sample with and without signs of disk activity. The theoretical evolutionary tracks of DM97 are given, where the horizontal solid lines are isochrones representing ages of 0.3, 1, 3, 10, 30, and 100 Myr and the main sequence, from top to bottom. The dashed line in the H-R diagram for the cloud core represents $K_{\rm dereddened} = 11$, which is the approximate completeness limit of the spectroscopic sample for $A_K < 3$.
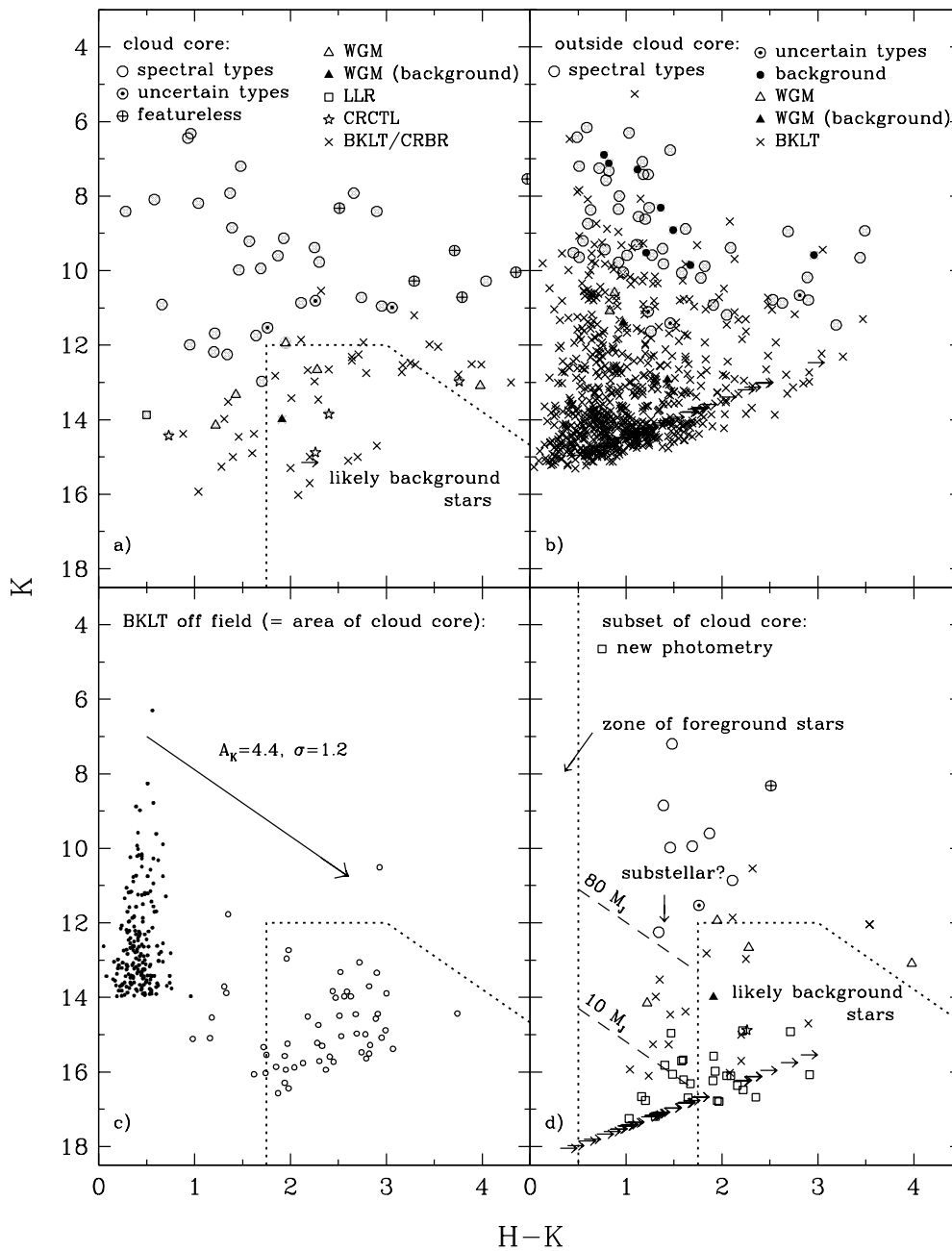
FIG. 10.—$H - K$ vs. K for the area (a) within the ρ Oph cloud core, as defined by the dashed boundary in Fig. 1, (b) that outside the cloud core and within Fig. 1, (c) an off field observed by BKLT equal in area to the cloud core, and (d) fields in the cloud core outlined by dotted lines in Fig. 1, which were observed at J, H, and K. In (a) and (b), we show sources classified through our K-band spectroscopy. Additional sources have been observed by WGM (K-band spectra), Luhman et al. (1997; optical spectrum), CRCTL (ISO photometry), and BKLT and CRBR (JHK photometry). The KLF (entire cloud core) and the HLF (subset of core) are consistent with a Gaussian reddening distribution ($A_K \sim 4.4$, $\sigma \sim 1.2$) toward the background stars behind the cloud core, which is simulated in (c) by reddening the off-field population. Consequently, the region enclosed by the dotted lines is where most background stars are expected to appear in (a) and (d). The dashed lines in (d) are the theoretical K magnitudes of substellar objects at 1 Myr (Burrows et al. 1997).

To interpret the H-R diagram of ρ Oph, several sets of low-mass evolutionary tracks are available. Luhman (1998), LR, and LRLL made comparisons of the D'Antona & Mazzitelli (1994, 1997, hereafter DM94, DM97) model predictions with observations of YY Gem and CM Dra, Pleiades, the main sequence, and globular clusters. Whereas calculations of both DM94 and DM97 were used in the analysis of data for IC 348 to provide continuity with previous studies, we will proceed with only DM97 in the following discussion.

As shown in Figure 9, the tracks of DM97 imply a median age of ~ 0.3 Myr for the cloud core, with a few stars older than 1 Myr, particularly at the lowest masses, where the scatter in apparent ages is largest. A similar range of ages is found in the sample surrounding the cloud core, where the median age is slightly older. A trend toward older ages with increasing distance from the cloud core is more obvious when these results are compared to the H-R diagram plotted by Greene & Meyer (1995) for optically visible stars observed across 3 deg²(Bouvier & Appenzeller

1992). Greene & Meyer also derived an H-R diagram for a sample observed with IR spectroscopy, composed of five stars from the core and 14 stars from the outer cluster. Using DM94, they found a distribution of ages very similar to that of the cloud core in Figure 9, although the study was slightly deficient in stars older than 1 Myr relative to the work presented here. Considering the uncertainties in model predictions and luminosity estimates at such early stages of evolution, absolute ages for these individual stars are not very meaningful. However, when the same set of evolutionary tracks is used from cluster to cluster, it is clear that ρ Oph is one of the youngest nearby stellar populations.

4.3. The Initial Mass Function
4.3.1. The Spectroscopic Sample

In conjunction with the evolutionary tracks of DM97, we can use $T_{\rm eff}$ and $L_{\rm bol}$ to estimate masses for individual sources in ρ Oph and construct a cluster IMF. Since the cloud core provides an excellent screen against background stars, cluster membership and completeness are more readily addressed, and we thus restrict the analysis of the mass function to sources within this region (see Fig. 1). Our spectroscopic sample contains 39 objects that fall within the cloud core. Seven sources (GY 6, GY 20B, GY 205, GY 254, GY 265, GY 214, and GY 227) exhibit heavily veiled, featureless spectra and are excluded from this calculation of the IMF. Photometry for the companion GY 20B is not available, and hence it is absent from the figures. Three sources in the cloud core, GY 192, $162712-243449$, and GY 192, had relatively uncertain late-type classifications and were not plotted in the H-R diagrams. They are indicated by circled dots in Figures 10 and 12. GY 192 has strong emission in $IRAS$ and $K-L'$ measurements and moderate excess in the $J-H$ and $H-K$ colors. We find that the spectral type ($>$M3) and luminosity estimate are consistent with the age of the cluster, implying a mass of $\sim 0.2\ M_\odot$. Strong excess emission in $H-K$ and $K-L'$ and weak K-band features are found in $162712-243449$. The spectrum of GY 128 is very noisy and quantitative measurements of its features are not possible. It also exhibits a flat-spectrum SED and a large $K-L'$ excess. Since $162712-243449$ and GY 128 cannot be classified and appear to be high-excess, heavily veiled objects similar to the seven featureless sources mentioned previously, they are omitted from the IMF. Two sources in our sample have uncertain reddenings and luminosities due to strong IR excess emission (GY 51) and a lack of J photometry (GY 244). By assuming these objects have ages comparable to the rest of the cloud core, we combined their spectral types with the evolutionary tracks to arrive at mass estimates. Because of uncertainties in the spectral types and subsequent mass estimates for two of the three early-type stars, the two highest mass bins are given widths of $\Delta \log M = 0.4$. For GY 182/WL 16 we use the H-band spectral type and a rough luminosity estimate to place it in the mass bin centered at $\log M = 0.35$ (1.4–3.5 $M_\odot$) (Biscaya et al. 1999). For the remaining 23 stars from our sample and six stars from WGM and Luhman et al. (1997) shown in the H-R diagram of the cloud core, individual masses were estimated with the evolutionary tracks. The two lowest mass bins were also doubled in width to compensate for the greater uncertainties in the evolutionary tracks and temperature scales in this regime.

The resulting IMF for the cloud core is composed of 36 sources, represented by the solid histogram in Figure 11.

4.3.2. Completeness Correction for $K \leq 13$

A completeness correction can be applied to the above IMF by (1) developing a model for the background stars shining through the cloud core at K, (2) identifying likely cluster members in the cloud core KLF that lack spectroscopy, and (3) estimating their masses by combining a canonical cluster age implied by the H-R diagram with photometry and evolutionary tracks. We have applied this approach previously in our studies of L1495E and IC 348 (LR and LRLL).

In the case of ρ Oph, we have obtained deep K-band images of the cloud core ($A_V \gtrsim 50$), covering the same region surveyed by CRBR (see Fig. 1). For the following discussion, we have merged our photometry with that of BKLT and CRBR. We use the data of BKLT when both H and K are provided ($H \lesssim 15.5$, $K \lesssim 15.0$), photometry of CRBR for the remaining sources detected in that work ($H \lesssim 17$, $K \lesssim 15.5$), and our new data for the faintest stars. The resulting set of photometry includes objects found
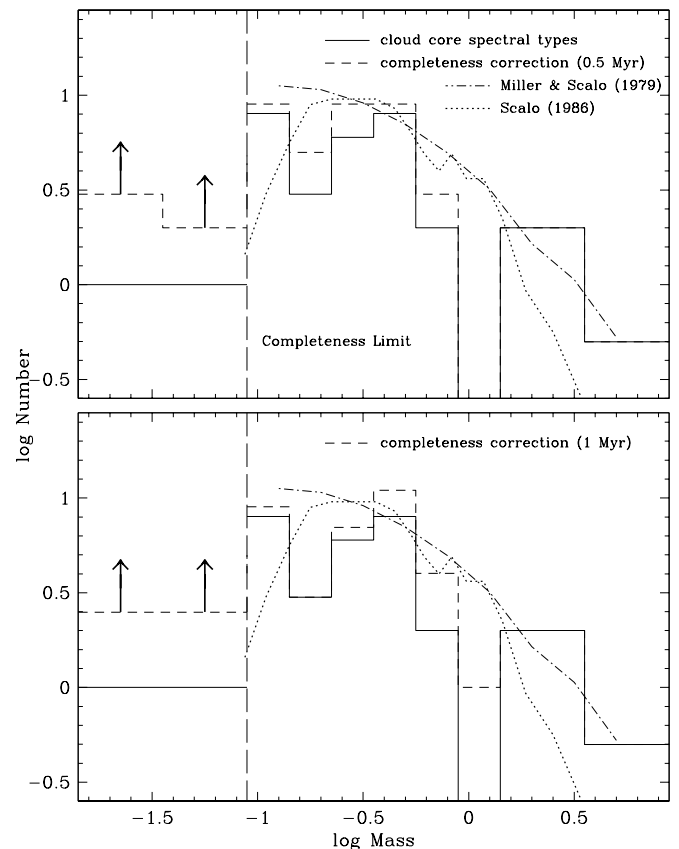

Fig. 11.—IMF derived from the cloud core spectroscopic sample with the evolutionary tracks of DM97 (*solid histogram*). All sources with featureless spectra are excluded from the IMF. The dashed histogram includes sources that (1) have uncertain late-type spectral types, (2) are identified as likely cluster members in *ISO* observations by CRCTL, or (3) lack spectra and are an excess above the background population in the KLF in Fig. 12. The completeness limit is indicated by the vertical dashed line and a lower limit to the substellar IMF is provided below this boundary. For reference, the field star mass functions of Miller & Scalo (1979) and Scalo (1986) are given. The two lowest and two highest mass bins were given widths of $\Delta \log M = 0.4$ because of uncertainties in mass estimates.

in our survey and in that of BKLT but not reported by CRBR: 162706−243811, 162713−243330, 162726 −244045, 162648−242836, and 162622−242254 (GY 12). The first four sources are faint companions to brighter objects, while GY 12 falls within bright nebulosity, explaining their absence from the photometry of CRBR. We reject five stars detected by BKLT that do not appear in our images or those of CRBR: 162718−243433, 162720−243820, 162703−243726, 162719−244156, and 162719−244122.

The cloud core KLF for the combined BKLT and CRBR data is given in Figure 12, in addition to the deeper extension provided by our data. It is evident from the rapid rise in counts at $K > 16$ that the new KLF reaches the background star population behind portions of the cloud core. To simulate this field population, we selected all BKLT sources within a $25' \times 10'$ area centered at $\alpha = 16^h24^m21\overset{s}{.}30$, $\delta = -24°42'00''$ (1950), which roughly equals the size of the cloud core. This position likely contains only relatively unreddened field stars, because it is near the outskirts of the BKLT survey where the molecular column density associated with ρ Oph is quite low. This off-field KLF must be reddened by $A_K \sim 3.75$ to fit the background star KLF ($K > 16$) observed toward the core. Such an average extinction is also consistent with the lack of background stars at $K < 12$ in the spectroscopic sample for the cloud core. The off-field KLF is fit well with a function of the form $N(m)$ $dm \propto 10^{\alpha m} \, dm$, where $\alpha = 0.31$, which is consistent with the

Galactic field distribution observed by Wainscoat et al. (1992). When a KLF of this form is reddened, Comerón, Rieke, & Neuhäuser (1999) found that the exponential form and value of α are preserved regardless of variable extinction or clumps. Thus, we show this fit to the background stars within the cloud core KLF in Figure 12. In a diagram of $H-K$ versus K in the third panel of Figure 10, we have reddened the off field by the best-fit extinction derived in § 4.3.5, illustrating where background stars should appear in the photometry.

Nine stars showing either little or no features and high excess emission were excluded from the IMF determination in § 4.3.1 since we could not constrain their spectral types or place them on the H-R diagram. Similarly, we do not attempt to add the high-excess, featureless objects to the IMF in the following completeness correction. Since many of the stars with no spectra at $K < 13$ have L-band measurements, we will reject objects with $K - L' \gtrsim 2$, which is typical of class I sources. The mass function derived from this analysis will be based on the assumption that these objects are not biased toward one mass regime. This assumption is consistent with recent optical spectroscopy of class I objects in Taurus, which exhibit a range of spectral types similar to that found among T Tauri stars (Kenyon et al. 1998a).

CRCTL detected mid-IR emission in *ISO* observations of low-mass candidates in the cloud core, several of which have been classified by WGM and Luhman et al. (1997) and
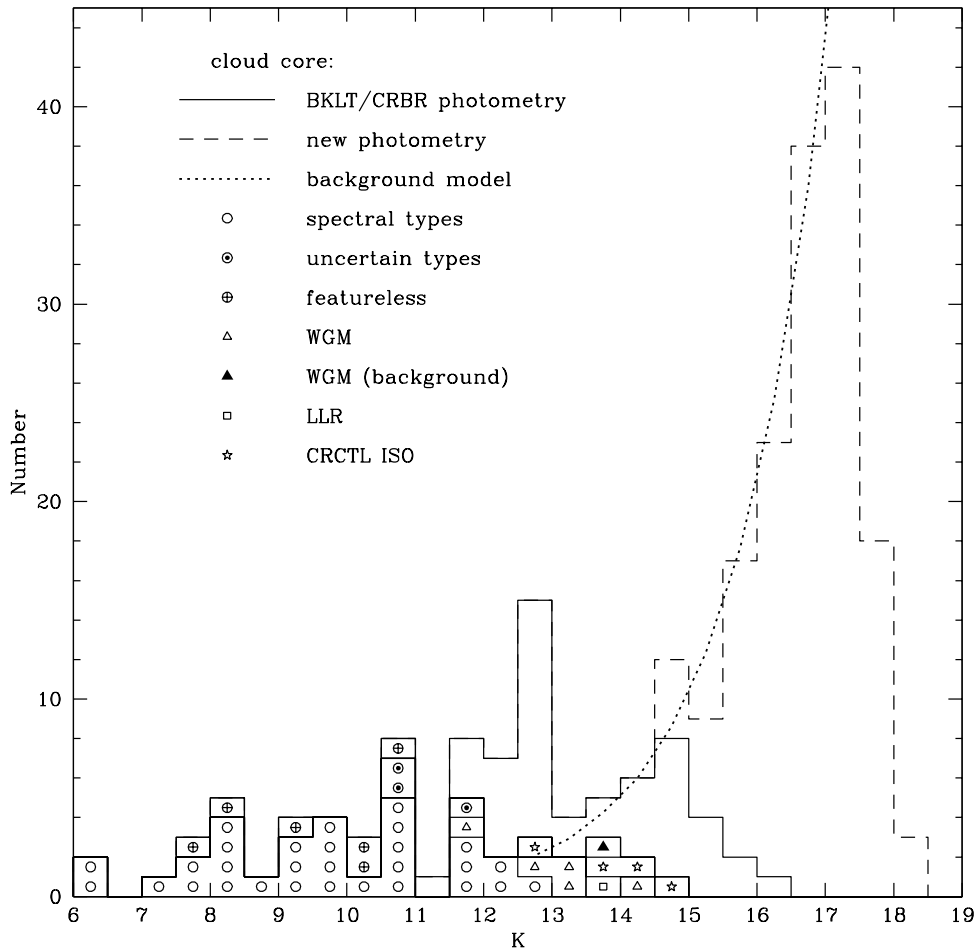

FIG. 12.—K-band luminosity function for the cloud core of ρ Oph. The dotted line is a model for the distribution of background stars

added to the IMF in § 4.3.1. The four remaining sources that lack spectroscopy show weak mid-IR excess emission and can be added to the IMF by the photometric modeling described below. These objects ($162623-242603$, $162653-243236$, $162710-242913$, and CRBR 33) are represented by the open stars in Figures 10 and 12.

The simulated background KLF predicts that only three stars in the $K = 12$–13 magnitude range are background. The cloud core KLF contains a number of sources in excess over the background model for $K = 11.5$–13. In addition, many of the objects between $K = 12$–13 have $H-K > 3$, much larger than expected for background stars, as shown in Figure 10. We therefore assume that all the objects with $K = 12$–13 are members of the embedded population, except for three we rejected that have plausible colors to be candidate background objects. Of these 19 remaining objects, nine show evidence for strong IR excess emission in $H-K$ or $K-L'$ and are excluded from the IMF modeling.

The remaining 10 sources are added to the IMF as a completeness correction in the following manner. As in § 3.2, extinctions are calculated by dereddening the $J-H$ and $H-K$ colors to the CTTS locus. When J photometry is not available, an intrinsic color of $H-K \sim 1$ is assumed, which is the maximum expected on the CTTS locus. Given the star formation history implied by the DM97 tracks in Figure 9, we assume canonical ages of 0.5 and 1 Myr for these 10 objects and convert the dereddened J (or H) magnitudes to masses for each age. After adding these photometrically derived masses to the IMF for the spectroscopic sample, we arrive at the distributions indicated by dashed lines in Figure 11. The completeness corrections for ages of 0.5 and 1 Myr are very similar. With the exception of the sources with large IR excess emission and featureless spectra omitted from the IMF, the final mass function for the cloud core is complete to $\sim 0.08~M_\odot$.

The derived IMF is only the primary star mass function. Although a large number of binary systems have been resolved (separation $>0\rlap{.}''005$) in lunar occultation observations of ρ Oph (Simon et al. 1995), our derivations include only companions that are detected in the images of BKLT and CRBR (separation $\gtrsim 1''$). Our IMF can be compared directly to results in other clusters, which generally also apply only to primary stars. As discussed by LRLL, under a broad range of assumptions, the inclusion of binary companions in the IMF produces a single star mass function with a low-mass slope of ~ 0.2–0.7 greater than that of the primary star mass function.

4.3.3. General Behavior of the IMF

At masses higher than $\sim 0.4~M_\odot$, the DM97 IMF for ρ Oph matches that of Miller & Scalo (1979), while falling less steeply than that of Scalo (1986). After the peak at $\sim 0.4~M_\odot$, the IMF slowly declines to the hydrogen-burning limit with a slope of ~ -0.5 in logarithmic units (where Salpeter is $+1.35$). The lower limits for counts of young brown dwarfs suggest that the slope is not significantly less than -0.5 from 0.02 to 0.4 $M_\odot$. Allowing for the errors and incompleteness below the hydrogen-burning limit, these results are consistent with the logarithmically flat IMFs between 0.05 and 1 $M_\odot$ estimated by CRBR and Strom et al. (1995) in IR luminosity function modeling of ρ Oph.

Using the tracks of Baraffe et al. (1997), Bouvier et al. (1998) have recently reported a slope of -0.4 for the low-mass IMF in the Pleiades, which agrees with our results in

ρ Oph and IC 348. LR, LRLL, and Scalo (1998) compared the IMFs measured near 0.1 $M_\odot$ in photometric and spectroscopic studies of young, open, and globular clusters. The new results for ρ Oph and the Pleiades further support their suggestion that these various regions do not show substantial variation in the low-mass IMF.

In comparison, recent discoveries of low-mass stars and brown dwarfs by 2MASS imply a present day field mass function that rises more rapidly with a slope of $+0.3$ (Reid et al. 1999). In addition, there appear to be significant differences in the mass functions derived between 0.5 and 2 $M_\odot$ among these studies. The Pleiades IMF of Bouvier et al. (1998) is broad and peaks at 0.6 $M_\odot$. Compared with this IMF, the populations in IC 348, ρ Oph, and Orion (Hillenbrand 1997) are deficient in stars near 1 $M_\odot$ and are peaked at $\sim 0.25~M_\odot$.

Some of these variations may be due to differences in the techniques and tracks used in the young clusters. For instance, the Pleiades data were converted to masses with theoretical relations of M_{bol}-mass ($>0.7~M_\odot$, DM97) and M_I-mass ($<0.7~M_\odot$; Baraffe et al. 1997), whereas spectral types and H-R diagrams were used for Orion (DM94), IC 348 (DM94; DM97), and ρ Oph (DM97).

4.3.4. Comparison to the Prestellar Clump Mass Function

The proximity and extreme youth of the ρ Oph star-forming region make possible the important comparison of the stellar IMF to the mass function of prestellar clumps. In deep millimeter-continuum observations of ρ Oph, Motte, André, & Neri (1998) have studied emission associated with circumstellar material, dense cores, and the ambient cloud. They detected 58 starless clumps that showed no radio or IR sources and appeared to be prestellar or protostellar in nature. After estimating individual clump masses, they constructed a mass function that exhibited a slope of ~ 1.5 for $\gtrsim 1~M_\odot$ and ~ 0.5 for $\lesssim 1~M_\odot$. Motte et al. noted the similarity to the field star mass function (e.g., Miller & Scalo 1979) and suggested a connection between the clump and stellar mass functions. Testi & Sargent (1998) have reached a similar conclusion in a study of Serpens. In this scenario, most of the mass in a given clump eventually accretes into a star or multiple system. With the new data presented here, we can now directly compare the stellar IMF for the ρ Oph cloud core to the clump mass function measured by Motte et al. (1998), as illustrated in Figure 13. Within the fairly low number statistics, the two mass functions are quite similar, providing further support for the notion that clump fragmentation directly influences the stellar IMF in a site of clustered star formation such as ρ Oph.

4.3.5. Using Reddening Models to Test Membership at $K > 13$

To explore the low-mass IMF further requires that we determine cluster membership for objects fainter than $K = 13$. Figure 10 shows that simple KLF modeling is inadequate for this goal. A number of faint ($K > 13$), relatively blue ($H-K < 1.75$) objects appear that may be low-luminosity cluster members rather than background stars. The isolation of these objects suggests that detailed modeling of the reddening that combines $H-K$ colors with the KLF may be more successful in probing for very faint cluster members.

There are discrepancies in the conclusions reached about the reddening in different studies. For example, CRBR confined their study to the region within the $A_V > 50$ contour
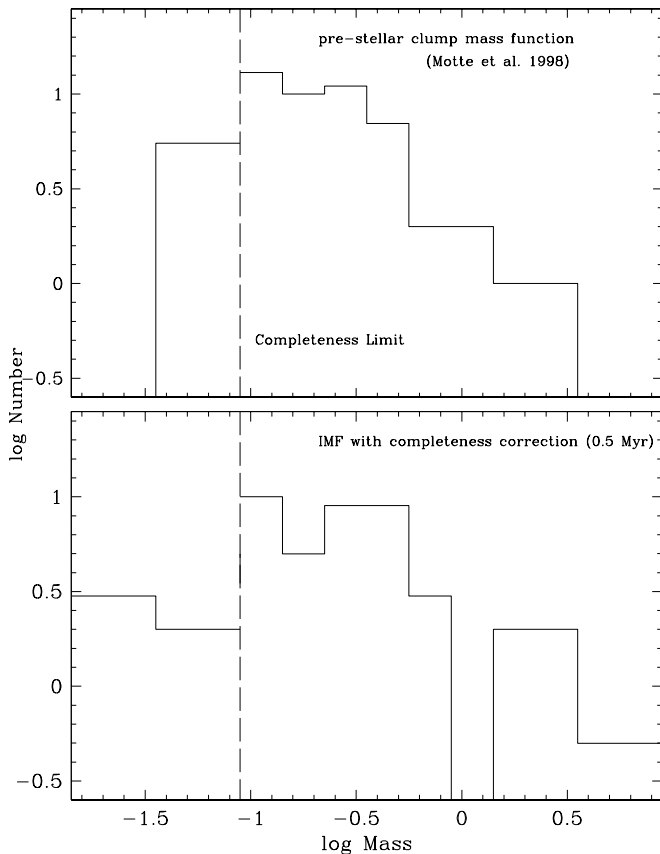
FIG. 13.—Prestellar clump mass function measured in ρ Oph from millimeter-continuum observations (Motte et al. 1998) and the cloud core IMF after a completeness correction assuming an age of 0.5 Myr (dashed line in lower panel of Fig. 11). The completeness limits of both studies are near 0.1 $M_{\odot}$.

in the CO maps of Wilking & Lada (1983). Based on a detailed discussion of the properties of the background reddened by this amount, they concluded that their sample included a number of background stars but not in a quantity that would significantly affect their results. In contrast, Kenyon et al. (1998b) used the $H-K$ versus $J-H$ color-color diagram to argue for an extinction only one-half as great as found from the CO maps, and they contend that CRBR may have sufficiently underestimated the contamination by background sources to affect their conclusions. Neither of these studies makes a quantitative determination of the effects of extinction variability on their conclusions. Variations within the CO beam would tend to increase the number of background sources seen through the cloud above the estimate by CRBR (as they point out). Variations will produce an underestimate of the average extinction in the color-color plot of Kenyon et al. (1998b), unless great care is taken to avoid selection effects against the redder sources.

With the availability of spectra and *ISO* data for many of the faint objects in the CRBR study (CRCTL; WGM; this paper), it appears indeed that most are bona fide embedded cluster members, in agreement with CRBR rather than Kenyon et al. (1998b). We still need to reconcile the derivation of strong background contamination by Kenyon et al. (1998b) and their determination of an extinction level less than one-half of that from CO maps and a "normal" ratio of CO column and A_V (Wilking & Lada 1983). One contrib-

uting factor is that BKLT and Kenyon et al. (1998b) included more area outside the $A_V = 50$ contour in their study than did CRBR. Another possibility is that extinction variations may have significantly affected the near-IR color distributions.

To pursue the latter question, we have used a simple model assuming a Gaussian distribution of extinctions. We have confined our study to the same area studied by CRBR. Most of this area lies within the CO-derived $A_V = 50$ contour. Our model can be used to take a background population and redden it in a manner that agrees with the observed properties of the background seen to be penetrating the ρ Oph obscuring cloud in our deep H and K images. From the background population appearing in off-cloud fields of BKLT, the cloud core KLF, and an assumption of uniform extinction, we had deduced $A_K \sim 3.75$ through the cloud (§ 4.3.2). However, in deep H-band images of selected regions within the cloud core, we found that the background begins to emerge at $H-K \sim 1.75$. This color is bluer than expected for the average level of $A_K \sim 3.75$, indicating that the extinction is nonuniform, so surveys at progressively shorter wavelengths are biased toward progressively less obscured members of the background.

We have two independent measurements to constrain the behavior of the extinction. First, by comparing the on-cloud and off-cloud star counts at K, we have determined the net effective extinction at that wavelength. Second, by imaging deep enough at both H and K to see the background population through the cloud, we have a measure of the bias discussed above. The interpretation of this bias is relatively simple at these colors, since plausible background stars all have nearly the same $H-K$ colors. We have assumed a uniform value of 0.15, which should be within about ± 0.1 of the color of most background stars (e.g., Leggett 1992).

We have modeled the extinction of the background assuming that the variations are Gaussian around an average value. We have taken a net $A_K = 3.75$ as a lower limit, to allow for the possibility that the "off" field we have used for comparison with the on-cloud field has some low level of extinction. We have assumed an upper limit of the net $A_K < 4.05$. From comparing the H and K luminosity functions, we find that the color difference at which the background emerges is $1.7 < H-K < 2.2$.

A range of parameters can fit the observed behavior within these limits. The true average extinction could lie from $A_K = 3.9$ with a standard deviation of 0.6 to $A_K = 5.0$ with a standard deviation of 1.45. A representative fit is $A_K = 4.4$ (i.e., $A_V \sim 40$) with a standard deviation of 1.2 (see Fig. 10), which is our best estimate of the true behavior of the cloud. Modeling the extinction variations has resulted in an increase by 10%–20% in the estimated average level. However, the possibility that the CO measures are slightly biased toward a high estimate is also confirmed.

Our extinction model also allows us to estimate the numbers of background sources we might see within our sampled region, as a function of $H-K$ (and K magnitude). The proportion is almost independent of K magnitude. The models with the largest background contamination are those with high average extinction, since the two-parameter fits then require large standard deviations for the extinction. For these "worst case" models, $\sim 16\%$ of the background stars would have $H-K < 1.5$, roughly independent of magnitude, and $\sim 9\%$ would have $H-K < 1.25$. Most of the successful models predicted significantly lower levels of blue

background star contamination; the values quoted are upper limits. These predictions are used in the following section to examine the status (reddened background stars vs. low-luminosity cluster members) of the very faint ($K > 14$), "blue" ($H - K < 1.5$) sources.

4.3.6. New Substellar Candidates

Figure 10 shows that we cannot achieve complete identifications of cloud members from the relatively blue ($H - K < 1.5$) colors discussed above; at the brighter levels, many bona fide members are redder than this limit. However, we can use the predictions to see if we are sampling a portion of the very low-mass cloud members. For example, between K of 13 and 16, there are 25 objects, of which nine are bluer than $H - K = 1.5$. Our background model would have predicted only four objects that blue. The range $K = 13$–16 corresponds to masses from about 0.01 to 0.08 $M_\odot$, so the presence of a significant number of objects in this range is consistent with our previous arguments that the IMF includes a reasonably large number of brown dwarfs at least down to 0.02 $M_\odot$.

Because of the small numbers of sources included in our deep survey in these magnitude ranges, this conclusion is not well established. Our main goal is to illustrate a method to extend cloud member identification to very low masses. One needs to image the cloud in at least two bands to a sufficient depth that the background stellar population is well characterized in both. The information on the background star color distribution allows construction of a model of the variations in extinction through the cloud. The modeling can be quite simple at H, K, and L because nearly all stars have similar intrinsic colors over these bands. Such a model can test whether relatively blue sources are likely to be cloud members as opposed to background sources shining through relatively thin sight lines of the cloud.

4.4. SED Classes and the First Stages of Stellar Evolution

Through low-resolution ($R = 500$) JHK spectroscopy, Greene & Lada (1996) examined the near-IR properties of a large number of young stars in ρ Oph and other star-forming regions. A range of IR SED classes was represented in their sample, including class I ($a > 0.3$), flat spectrum ($0.3 \geq a \geq -0.3$), II ($-0.3 > a \geq -1.6$), and III ($a < -1.6$), where a is the mid-IR spectral index (Lada 1987; Greene et al. 1994). This index measures the slope of an SED from 2 μm to 10–20 μm and is sensitive to the presence of cool circumstellar material. Greene & Lada observed a trend of increasing line emission and reddening in addition to weakening absorption lines from class III to class I sources, consistent with the evolutionary interpretation of these observational classes. Our results on the relationship between veiling and location on the $H - K$ versus $J - H$ diagram shown in Figure 7 confirm these arguments. In addition, we find a decreasing incidence of detectable Brγ emission with decreasing IR excess, as expected.

By combining previous near- and mid-IR photometry with our measured spectral types, continuum veilings, and emission-line strengths, we now investigate in more detail fundamental questions regarding the evolution of young stars. For instance, are some objects previously identified as class I in fact older and partially emerged from their natal dust shells but so heavily reddened by the molecular cloud that their SEDs place them in class I? With these data, we will (1) deredden the spectral indices and review the SED

classifications, (2) calculate the timescale for the class I protostellar stage of evolution, (3) use our spectroscopic data to constrain the origin of IR excess emission in class I and class II objects, (4) estimate the detectability of absorption features in spectra of class I sources, (5) discuss the nature of the reddening in class II sources, and (6) compare the distribution of SED classes inside and outside of the ρ Oph cloud core.

4.4.1. Revised SED Classifications

To sort the ρ Oph sources into SED classes requires a determination of their intrinsic $K(2.2\ \mu\text{m}) - N(10.6\ \mu\text{m})$ spectral indices. We have done so for a sample of all sources with $K < 12$ that have spectral types of K1 or later or exhibit featureless K-band spectra. The multiple systems GY 20 and GY 240 are not included since the components are unresolved in the mid-IR data. IRAS 64A, the possible background and foreground stars, and several sources with uncertain late-type classifications are also omitted.

Ground-based mid-IR measurements were taken from Elias (1978), Lada & Wilking (1984), Young, Lada, & Wilking (1986), Wilking et al. (1989), and Greene et al. (1994). Two objects were classified with the *ISO* observations of CRCTL. We avoided *IRAS* measurements because the beam is large enough that confusion with a fainter and redder object is a possibility. We have used these data with the values of A_J and K in Table 1 to compute the extinction-corrected $K - N$ (2.2–10.6 μm) spectral indices given in Table 2. When available, $a(2.2$–20 μm) and measurements of continuum veiling and Brγ emission from the K-band spectra are also listed.

Stars within the reddening bands of the main sequence and CTTS locus should have reasonably accurate extinction estimates, so for them we have relied on the dereddened indices in classifying their SEDs. When mid-IR data were available but extinctions could not be computed because of the lack of J-band photometry, the sources were classified by considering both the observed index and r_K. For sources to the right of the CTTS locus, scattered light may dominate and the reddenings are uncertain, so we make no attempt at dereddening their spectral indices. GY 6, GY 111, GY 214, GY 254, GY 265, GY 269, GY 274, and GY 378 fall in this category and are likely true class I rather than heavily reddened class II objects, given their strong veiling and steep SEDs between 2 and 20 μm. GY 205, GY 224, and GY 227 are flat-spectrum sources by their observed indices, which cannot be dereddened reliably because of large $H - K$ excess (GY 205) and lack of J photometry (GY 224 and GY 227). The spectra of these three objects are featureless, supporting their flat-spectrum status, although the low signal-to-noise ratio provides weak constraints on the veiling ($r_K > 0.5$). Because GSS 26, GY 21, GY 51, GY 279, and GY 315 are within the CTTS reddening band or a small distance to the right of it, we can calculate dereddened spectral indices. Although the dereddened indices for GSS 26, GY 21, and GY 51 indicate class II, they remain close to the flat-spectrum regime, so we cannot confidently classify these as either flat or class II. Similarly, GY 279 and GY 315 are likely class II, but we cannot rule out flat-spectrum status because of variability in GY 279 and uncertain extinction in GY 315. No mid-IR photometry is available for GY 81, but comparing the spectroscopic properties to those of the sources we have discussed, it is probably flat spectrum or class II. Other sources

TABLE 2
SED Classifications and Spectroscopic Data

| ID | a (2–10 μm)[a] | | CLASS[b] | OTHER DATA[c] | | |
	Observed	Dereddened		r_K	Brγ (Å)	a (2–20 μm)
GY 6	1.2	...	I	>2	2.0 ± 0.2	$a20$ = 1.3
GY 111	1.2	...	I	1–3	1.8 ± 0.4	$a20$ = 0.9
GY 214	1.2	...	I	>2	3.0 ± 0.1	$a20$ = 0.9
GY 254	1.0	...	I	>1	6.2 ± 0.4	$a20$ = 0.6
GY 265	0.7	...	I	>1	1.5 ± 0.7	$a20$ = 0.9
GY 269	1.4	...	I	1	...	$a20$ = 1.6
GY 274	1.4	...	I	>1	2.0 ± 0.6	$a20$ = 1.1
GY 378	2.7	...	I	>2	4.3 ± 0.4	$a20$ = 2
GY 205	0.3	...	Flat	>0.5	5.9 ± 0.4	$a20$ < 0.4
GY 224	0.2	...	Flat	>0.5	8.5 ± 1.0	$a20$ = 0.1
GY 227	0.2	...	Flat	>0.5	...	...
GSS 26.......	0.3	−0.4	Flat/II	4, 0.75	2.9 ± 0.2, 1.7 ± 0.3	$a20$ = −0.1
GY 21........	0.0	−0.5	Flat/II	1[d]	2.0 ± 0.7	...
GY 51........	0.3	~ −0.4	Flat/II	2, 0.5	5.0 ± 0.5, 1.5 ± 0.5	...
GY 279	−0.2, 0.3	−1.0, −0.5	Flat/II	0.75, 1[d]	...	$a20$ = 0[e]
GY 315	0.2	~ −0.9	Flat/II	1–3	2.0 ± 0.6	$a20$ = 0.1
GY 81........	...	...	Flat/II?	1–2	3.0 ± 0.5	...
EL 24	−0.7	−0.9	II	1–3	2.7 ± 0.2	$a20$ = −0.6
GSS 28........	−0.8	−0.9	II	0.5	1.9 ± 0.15	...
GSS 29.......	−0.8	−1.2	II	0	...	$a20$ < −0.8
GY 23........	−0.5	−0.9	II	0.75	...	$a20$ = −0.6
GY 110	−1.1	−1.5	II	0.25	0.6 ± 0.2	...
GY 116	−0.7	−1.3	II	0.75	2.1 ± 0.15	...
GY 129	−1.1	−1.4	II	>1	13.7 ± 0.5	...
GY 167	−0.6	−0.7	II	1–3	4.7 ± 0.15	$a20$ = −0.3
GY 168	−0.6	−0.8	II	2	1.3 ± 0.2	$a20$ = −0.5
GY 211	−1.0	−1.4	II	0.75	...	$a20$ < −0.3
GY 244	0.3	−1?[g]	II?	0	...	$a20$ < 0.5
GY 247	−0.9	−1.5	II	0.25	...	$a20$ < −0.9
GY 267	−1.1	−1.5	II	0.25	...	...
GY 273	−0.3	−1.0	II	0	...	$a20$ < −0.1
GY 292	−0.8	−1.1	II	1	1.0 ± 0.4, 3.0 ± 1	...
GY 308	−0.7	−1.1	II	0.75	0.8 ± 0.2	...
GY 314	−0.8	−1.1	II	0.5	1.6 ± 0.3, <0.5	...
GY 319	−1.3	−1.3	II	0.75	...	$a20$ = −1.1
GY 400	−1.1	−1.1	II	0.5	2.5 ± 0.3	...
SR 4..........	−1.0	−1.1	II	1.5, 2, 1.5	6.7 ± 0.3, 4.5 ± 0.5, 5.5 ± 0.5	$a20$ = −0.7
IRS 2..........	−1.4	−1.6	II	0	...	...
WSB 60.......	−0.4	−0.5	II	0.75	...	...
GSS 20........	< −1.9	< −2.0	III	0	...	...
GSS 23........	−2.1	−2.3	III	0	...	$a20$ < −1.6
GY 5	~ −1.5[h]	~ −1.9[h]	III	<1	...	...
GY 12.........	< −2.0	< −2.6	III	0	...	...
GY 17.........	−1.9	−1.9	III	0	0.9 ± 0.2	...
GY 29.........	...	...	III?[f]	0	...	...
GY 37.........	...	...	III?[f]	?	...	...
GY 59.........	...	...	III?[f]	?	...	...
GY 84.........	...	...	III?[f]	0	...	...
GY 135	< −2.1	< −2.6	III	0	...	...
GY 153	−0.9	−1.7	III	0.25	1.7 ± 0.4	...
GY 156	< −2.2	< −2.9	III	0	...	...
GY 172	<0.6	<0.0	III?	0	...	$a20$ < 1.1
GY 250	< −2.10	< −2.12	III	0	...	...
GY 253	< −1.2	< −2.1	III	0	...	...
GY 262	−1.5	−2.3	III	1	2.2 ± 0.3	...
GY 284	...	...	III?[f]	0	...	...
GY 295	< −2.2	< −2.4	III	0	...	...
GY 306	< −1.35	< −1.73	III	0	...	...
GY 310	...	...	III?[f]	...	...	...
GY 326	...	...	III?[f]	...	...	...
GY 410	< −1.7	< −2.0	III	0	...	...
GY 93.........	−1.7	−1.8	III	0	...	...
LFAM 8	...	...	III?[f]	0	...	...
ROXs 39......	−2.6	−2.6	III	0	...	...

TABLE 2—*Continued*

	a (2–10 μm)[a]			OTHER DATA[c]		
ID	Observed	Dereddened	CLASS[b]	r_K	Brγ (Å)	a (2–20 μm)
SR 20	−1.6	−1.8	III	1	...	...
VSSG 11	< −1.12	< −1.62	III	0	...	...
VSSG 22	< −1.6	< −2.2	III	0	...	...
SR 22	−1.6	−1.7	III	0.25	1.9 ± 0.4	...
WSB 38	−1.6	−1.9	III	0.75	0.6 ± 0.15	...
162559−242124	...	...	III?[f]	0	...	...
162615−241924	...	...	III?[f]	0	...	...
162618−242416	∼ −0.2[i]	∼ −2.0[i]	III?	...	...	...

[a] Data taken from Elias 1978, Lada & Wilking 1984, Young et al. 1986, Wilking et al. 1989, and Greene et al. 1994.

[b] SED classification (Greene et al. 1994) based on a(2–10 μm) and the other data given (see § 4.4.1).

[c] Continuum veiling and W_λ(Brγ) measured in the K-band spectra and the spectral index from 2–20 μm when available.

[d] Greene & Lada 1997.

[e] Measurement of 20 μm photometry was at the same epoch as the 10 μm data used in a10 = 0.3.

[f] Tentative SED classification based on JHK colors and veiling in the K-band spectra.

[g] Dereddening is based on the assumption that $H − K$ is not affected significantly by excess emission, as suggested by $r_K \sim 0$ measured in the spectrum.

[h] a(2–6.0 μm).

[i] a(2–4.5 μm).

without mid-IR data are tentatively classified in a similar fashion. We have no J photometry for GY 244, but the lack of veiling or Brγ emission implies little excess at K, so we estimate the extinction from $H − K$. The dereddened spectral slope indicates that GY 244 may be a heavily reddened class II object.

For calculating the distribution of sources across SED classes, we divide the six objects labeled as flat/II equally between flat spectrum and class II and consider flat spectrum a part of class I. With the revised classifications, there are 12.5, 26.5, and 33 sources among class I, class II, and class III, respectively. The dereddening has moved 18%–30% (8–13/44) of sources that are class I or class II by the observed indices from one class to another, in contrast to the suggestion of Greene et al. (1994) that less than 10% of sources should change SED classes upon dereddening. These discrepant conclusions may be caused by differences in how the dereddened indices were calculated in the two studies. Greene et al. state that a(2–10 μm) changes by 0.5 when reddened by $A_V = 50$ under the extinction law of Rieke & Lebofsky (1985), whereas we find the change in the index is 1.7.

Selection effects will influence these results. For example, an object of a given mass is expected to fade in bolometric luminosity between class I and class III, favoring the detection of the class I stage. However, it is also possible that a smaller portion of the luminosity emerges in the near-IR because of the larger extinction in the class I phase, favoring the detection of the later classes in our K-band–limited sample. For instance, five of seven sources classified as class I or flat spectrum by Greene et al. (1994) have $K > 12$ and therefore are not included in the statistics we have discussed. Disks around very young objects where the dust has not started to coagulate or dissipate may hide the object from near-IR surveys along some sight lines. For example, if the mass of the planets in the solar system were distributed uniformly in a disk of 100 AU radius and 3 AU thickness, the density would be of order 10^{-14} g cm^{-3}, corresponding to $A_J \sim 1000$ taking typical interstellar parameters. Unresolved binaries will tend to favor class II designation. In the

case of a class II source paired with a class III one, the mid-IR excess would bias the composite to class II. A class II or III source paired with a class I one would produce composite near-IR characteristics (photospheric absorptions, bluer $K − N$ color) indicative of class II. Nonetheless, the ratios of the numbers of sources in the various classes should give a rough idea of the true distribution among the SED classes.

4.4.2. *Timescale for the Protostellar Stage*

A variety of arguments regarding the very early development of a young star assign probable durations to the stages corresponding to differing SED characteristics. Specifically, it is thought that the class I SED type should persist for only 0.1–0.2 Myr (e.g., Cohen & Kuhi 1979; Stahler 1983; Shu, Adams, & Lizano 1987). However, the photometric surveys of CRBR and Greene et al. (1994) have found class I objects in larger numbers than this short duration would suggest.

However, after dereddening the sources and extracting statistics from a magnitude-limited sample, only about 17% (12.5/72) of them are class I. This proportion is substantially lower than previous estimates (CRBR; Greene et al. 1994). If we interpret the proportion of class I sources as an indication of the lifetime of that phase of stellar evolution and assume that star formation has occurred at a uniform rate over the last 0.5–1 Myr in the ρ Oph region, then the lifetime of the embedded stage is ∼0.075–0.15 Myr. This estimate removes the discrepancy with theoretical expectations found in previous estimates of the proportion of class I sources.

4.4.3. *Nature of Infrared Excess Emission in Classes I and II*

In a generally accepted view of the protostellar stage, the class I SED has been modeled as a star surrounded by an accretion disk and a thick circumstellar envelope, where the disk is thought to contribute a substantial portion of the excess emission at 10 μm (Myers et al. 1987). Because of the lack of disk absorption features in class I and II systems, Calvet, Hartmann, & Strom (1997) have suggested that the

stellar magnetosphere induces a hole in the inner region of the disk, thus preventing the formation of a disk photosphere. They propose that a warm infalling envelope dominates circumstellar excess at 2 μm. In a class II object where the envelope is absent and only the disk remains, relatively little K-band continuum emission ($r_K \lesssim 1$) is predicted (Meyer et al. 1997). We now consider this model in light of the new data we present.

In 1996 May, GSS 26 and GY 51 (flat/II) exhibited strong Brγ emission (2.9 ± 0.2, 5.0 ± 0.5 Å) and veiling ($r_K \sim 4$, 2), while in 1994 July the Brγ emission was weaker (1.7 ± 0.3, 1.5 ± 0.5 Å) and the excess was lower ($r_K \sim 0.75$ and 0.5). Furthermore, when these spectra are flux calibrated, we find that GSS 26 and GY 51 were ~1.2 and 1.3 mag brighter at K in 1996 relative to 1994, consistent with the increase in excess continuum emission implied by r_K. Both the excess emission and Brγ line flux in each star brightened by factors of 5–10. If the Brγ emission arises in columns of material accreting from the disk onto the star (Muzerolle, Calvet, & Hartmann 1998), then the simultaneous increase in the Brγ emission and the continuum veiling suggests that the excess emission is produced in a region directly associated with the accreting material (i.e., the disk) rather than a circumstellar envelope.

We can also use the behavior of r_K with changing SED class to probe the origin of the excess emission. If an infalling envelope is responsible for the significant continuum veiling at 2 μm seen in a given source, strong mid- and far-IR emission should also be generated, appearing as a class I SED. However, we find strong veiling, $r_K = 1$–4, in several sources lacking this evidence of an envelope, as shown in Table 2. Examples include GSS 26, GY 21, GY 51, GY 279, and GY 315, which are possibly class II after dereddening. Even without dereddening, EL 24 ($r_K = 1$–3), GY 129 ($r_K > 1$), GY 167 ($r_K = 1$–3), GY 168 ($r_K = 2$), GY 292 ($r_K = 1$), and SR 4 ($r_K = 1.5$–2) are class II, yet they have moderate to heavy veiling. Finally, we measure $r_K = 1$ in GY 262 and SR 20, which show no sign of an envelope by their class III status. On the other hand, a disk is likely to be present in all of these SED classes. If the disk is the source of the K-band excess emission, then the inner hole must be within the region where dust would emit strongly at 2 μm while large enough to prevent dust destruction and the resulting formation of a substantial disk photosphere. The central hole in the model by Greene & Lada (1996) was tuned in this manner and produced veilings of $r_K \lesssim 1$ for a pure reprocessing disk and $r_K \lesssim 5$ for a luminous disk, although this choice of hole size has been subsequently criticized by Calvet et al. (1997) as nonphysical.

4.4.4. Detecting Absorption Features in Class I Sources

In addition to class II and class III sources, can photospheric features also be detected in extremely red objects designated as class I? Greene & Lada (1997) observed absorption features in two sources, GY 21 and GY 279, and demonstrated that the lines likely originate in the photospheres of the central stars rather than disks. Although these objects were previously classified as flat spectrum, they appear to be class II when their spectral indices are dereddened (see § 4.4.1). With our large set of moderate-resolution spectra, we can further examine the detectability of absorption features in flat-spectrum and class I sources. Featureless K-band spectra are found for GY 6, GY 20B, GY 214, GY 254, GY 265, GY 274, GY 378 (class I), GY

205, GY 224, GY 227 (flat spectrum), and GY 129 (class II). However, absorption features are detected in the class I objects GY 111 and GY 269, comprising about ~25% of class I sources. Since the signal-to-noise ratio is rather low in some of the featureless spectra, higher quality data could reveal absorption features in still more of the class I stars.

4.4.5. Nature of the Reddening in Class II Sources

To test the origin of the obscuration for the highly reddened class II objects, we have computed the average A_J for the class II and class III sources in the sample described here. The ratio $A_J(\text{II})/A_J(\text{III}) = 1.1 \pm 0.2$; thus there is no excess of extinction for class II objects. The distribution of extinction values is also similar between the classes. Thus, the class II and III sources appear to be distributed throughout the cloud in a similar fashion, as one would expect. This result supports our conclusion that some sources previously considered to be of class I or II are instead heavily reddened class II or III. In addition, any circumstellar disks around class II objects appear to have little influence on the extinction—either the disks are optically thin at J, or they are thick enough that systems oriented with their disks edge on are so heavily obscured that we do not detect them.

4.4.6. Spatial Distribution of SED Classes

We now make a comparison of the IR characteristics of the areas separated by the dashed line in Figure 1, defining stellar populations from the cloud core and the surrounding region. In the diagrams of $H - K$ versus $J - H$ in Figure 8, we find that a larger fraction of sources within the cloud core have near-IR excess emission. To be more quantitative, we designate sources with evidence for actively accreting circumstellar disks as those exhibiting $W_\lambda(\text{Brγ}) > 1$ Å or $r_K \geq 0.5$. In the core of ρ Oph, if we omit the B star and seven sources with uncertain veiling measurements, the frequency of disks is 17/27 (63%). The frequency is somewhat lower outside of the cloud core, 23/45 (51%), after omitting the four earliest stars, two K-M stars, IRAS 64A, and the foreground and background stars. The difference between the two populations is more pronounced when we examine the SEDs. For sources in the cloud core that have been classified in Table 2, the number distribution among class I/flat, class II, and class III is 6.5, 9.5, and 10, respectively. Outside of the cloud core, on the other hand, the SEDs are generally more evolved, where the distribution is 6, 17, and 23.

In a study of the older cluster IC 348 (0.5–10 Myr) by LRLL, ~24% of sources within the core with ages less than 3 Myr met the $W_\lambda(\text{Brγ}) > 1$ Å or $r_K \geq 0.5$ criterion for active accretion. The lower fraction of disk sources in the core of IC 348 relative to the remainder of cluster was attributed to the accelerated truncation of disks at higher stellar densities (Herbig 1998; LRLL). In ρ Oph, since the densities are rather low throughout the region, the higher disk frequencies from the core outward are instead likely due to the birth of stars in the cloud core and their dispersal outward. Such an age gradient is consistent with the ages implied by the H-R diagram of the cloud core and surrounding area, as discussed in § 4.2.

5. CONCLUSION

We have performed K-band spectroscopy toward ~100 stars within the ρ Oph star-forming region. We have mea-

sured spectral types and continuum veilings and have combined this information with previous mid-IR measurements and new near-IR imaging of the cloud core. Our conclusions are as follows.

1. The K-band steam absorption, known to strengthen rapidly with from mid-M to M8 V and possibly to saturate for later types, is also sensitive to surface gravity and differs between ~ 1 Myr and the main sequence for a given spectral type. Thus, young late-type objects classified in the optical should be used as spectroscopic standards when using steam to measure spectral types for young, cool objects.

2. Using the evolutionary tracks of DM97 to interpret the H-R diagram for ρ Oph, we estimate stellar ages ranging between 0.1 and 1 Myr, with a few stars that may be slightly older.

3. From a deep KLF of the cluster core, we develop a reddening model for the background star population and identify likely cluster members falling below the limit of the spectroscopic sample. We use the age from the spectroscopic sample to convert their luminosities to masses. After the addition of these sources, the resulting IMF is complete to $\sim 0.08\ M_\odot$. With the tracks of DM97, the IMF for ρ Oph matches that of Miller & Scalo (1979) at masses higher than 0.4 $M_\odot$. The IMF peaks at this mass and slowly declines to the hydrogen-burning limit with a slope (in logarithmic units) of ~ -0.5, as compared to slopes of $+1.35$, 0, and -2.6 for Salpeter (1955), Miller & Scalo (1979), and Scalo (1986), respectively. The exact shape of the mass function remains dependent on the theoretical evolutionary tracks and temperature scales.

4. Our lower limits on the numbers of substellar objects demonstrate that the IMF probably continues a slow decline and does not fall precipitously below the hydrogen-burning limit, at least down to $\sim 0.02\ M_\odot$.

5. The derived IMF is consistent with previous findings that the ρ Oph IMF is roughly flat from 0.05 to 1 $M_\odot$.

6. The stellar IMF in ρ Oph is qualitatively similar to the mass function of prestellar clumps, indicating that cloud fragmentation may play a direct role in determining the IMF.

7. Very deep imaging at H and K (also at L) can be used to construct models of the extinction through the cloud and to determine background contamination as a function of color and magnitude. We have used this method in a limited area to identify several faint sources ($K = 13$–16) that may be cluster members by their low reddenings ($H - K < 2$) and thus are low-mass substellar candidates.

8. Extinction can significantly alter the true distribution of SED classes. The classifications of $\sim 25\%$ of sources originally classified as class I–II are changed upon dereddening of the mid-IR indices [$a(2$–10μm)]. After revising the SED classification accordingly, $\sim 17\%$ of the ρ Oph stars are class I, implying ~ 0.075–0.15 Myr for the lifetime of this embedded stage.

9. We detect absorption features in the spectra of $\sim 25\%$ of class I and flat-spectrum sources, supporting the feasibility of studying the photospheres of extremely young protostars.

10. In observations of 20 sources separated by 2 yr, we find that the continuum veiling and Brγ emission change simultaneously in two stars. Because the Brγ emission likely traces material in the accretion columns between the disk and the star, this behavior suggests the disk as the origin of the 2 μm excess rather than an infalling envelope. The presence of significant veiling ($r_K = 1$–4) in the spectra of several stars from flat spectrum to class III also indicate that a disk, or at least something other than an envelope, is capable of producing large amounts of continuous 2 μm emission.

11. The IR properties of the sample imply a slightly more evolved population distributed around the cloud core, possibly because of the birth of stars within the core and their subsequent dispersal, which is also consistent with the ages implied by the H-R diagrams of the cloud core and surrounding region.

APPENDIX A

NOTES ON INDIVIDUAL SOURCES

With the exception of RNO IC, which is similar to the data for the K2 III κ Oph (Kleinmann & Hall 1986), the K-band spectra of FU Ori objects are all similar and show characteristics distinct from normal stars, as shown in Figure 14. Some of this difference is likely due to broadening of lines from disk rotation (Greene & Lada 1997). The FU Ori spectra also show two features on either side of where Mg appears in the giant (possibly the two lines seen in late M dwarfs) and unidentified absorption at 2.33 μm. All of these characteristics are found in the spectrum of IRAS 64A. While the FU Ori objects have strong CO absorption and late-type IR spectra, they tend to appear as F or G giants in the optical. This discrepancy is reconciled by attributing the CO to absorption in low-gravity disk atmospheres. However, we find that the optical spectrum (6000–9000 Å) of IRAS 64A is identical to the M8–M9 III spectra presented by Kirkpatrick, Henry, & Irwin (1997). High-resolution spectroscopy on the CO band heads is necessary to determine whether a circumstellar disk is the origin of these peculiar optical and IR spectra.

Another unique source, GY 182/WL 16, is well-known for its strong CO band head emission, modeled successfully in terms of an inversion layer in a circumstellar disk (Carr et al. 1993; Najita et al. 1996). As seen in Figure 6, no photospheric features appear in the K-band spectrum of this class I object. However, in observations of second-overtone CO emission, Biscaya et al. (1999) detect absorption in the H-band Brackett series of hydrogen, presumably arising from the stellar photosphere of the
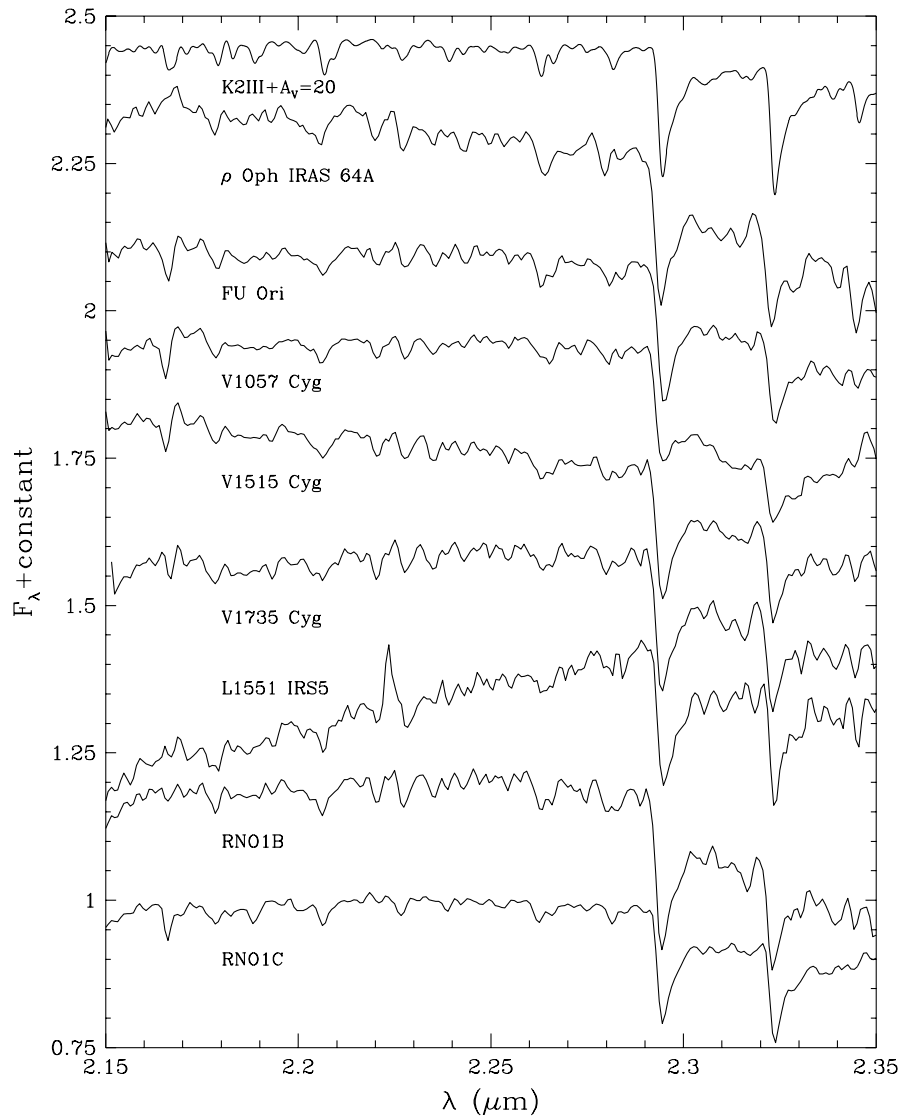
FIG. 14.—K-band spectrum of IRAS 64A compared to data for several FU Ori objects and a typical field K giant (reddened by $A_V = 20$). Spectra are normalized at 2.2 μm with constant offsets.

central star. They conclude that the spectral type of WL 16 is between B8 and A7 ($T_{\rm eff} = 8000$–12,000 K). Subsequent modeling of the CO emission further constrains the temperature of the star to be 9000 to 12,000 K.

GY 20/DoAr 24E is a binary system with a separation of 2″06 and component magnitudes of $K = 6.9$ and 7.9 (Simon et al. 1995). The curvature in the slope of the class I secondary is due to its proximity to the primary and the resulting difficulties in extracting the spectrum. Since the companion is much redder than the primary, we assume that the BKLT J photometry applies to only GY 20A when deriving the luminosity.

For GY 29, both the CO bands and the shape of the continuum produced by steam absorption match well with the spectrum of V410 X-ray 6 (M5.5) artificially reddened by $A_V = 25$.

In addition to absorption in Brγ, we clearly detect weak features of Na, Ca, and CO in the B star GY 70/S1. The source of these metal lines is likely the fainter, unresolved secondary ($\Delta K = 1.8$, 0″02, Simon et al. 1995).

GY 240/WL 20 is a triple system (BKLT, references therein) appearing as one source in the data of BKLT and Wilking & Lada (1983) and two sources separated by 2″–3″ in the images of CRBR and Barsony et al. (1989). We refer to the west and east components as GY 240A and B. Since GY 240B has no J photometry and the $H - K$ colors of the two sources are similar, we derive the extinction from BKLT $J - H$ for the composite system and assume it applies to each component. To estimate a J magnitude for the individual sources, we assume a difference of ~ 1.2 mag, which is measured by CRBR at H and K.

GY 250/SR 12 is a binary system with a separation of 0″3 and component magnitudes of $K = 9.3$ and 9.4 (Simon et al. 1995). We assume the components have the same spectral types and divide the luminosity in half. Only one source is added to the IMF, for reasons discussed in § 4.3.2.

GY 372/VSSG 14 is an unresolved binary system (0″1; Simon et al. 1995) in which the secondary is 0.8 mag fainter at K. As with GY 70/S1, Brγ is strong, while we also detect absorption in metal lines and CO that may arise in the secondary. Because of possible line and continuum veiling (from either the secondary or IR excess emission), the classification of the primary is uncertain ($<$F8).

REFERENCES

Allard, F., & Hauschildt, P. H. 1995, ApJ, 445, 433
Baraffe, I., Chabrier, G., Allard, F., & Hauschildt, P. H. 1997, A&A, 327, 1054
Barsony, M., Burton, M. G., Russel, A. P. G., Carlstrom, J. E., & Garden, R. 1989, ApJ, 346, L93
Barsony, M., Kenyon, S. J., Lada, E. A., & Teuben, P. J. 1997, ApJS, 112, 109 (BKLT)
Biscaya, A. M., Calvet, N., Rieke, G. H., & Luhman, K. L. 1999, in preparation
Bouvier, J., & Appenzeller, I. 1992, A&AS, 92, 481
Bouvier, J., Stauffer, J. R., Martín, E. L., Barrado y Navascués, D., Wallace, B., & Bejar, V. J. S. 1998, A&A, 336, 490
Briceño, C., Hartmann, L., Stauffer, J., & Martín, E. L. 1998, AJ, 115, 2074
Burrows, A., et al. 1997, ApJ, 491, 856
Calvet, N., Hartmann, L., & Strom, S. E. 1997, ApJ, 481, 912
Carr, J. S., Tokunaga, A. T., Najita, J., Shu, F. H., & Glassgold, A. E. 1993, ApJ, 411, 37
Casali, M. M., & Eiroa, C. 1996, A&A, 306, 427
Casali, M. M., & Matthews, H. E. 1992, MNRAS, 258, 399
Casanova, S., Montmerle, T., Feigelson, E. D., & André, P. 1995, ApJ, 439, 752
Cohen, M., & Kuhi, L. V. 1979, ApJS, 41, 743
Comerón, F., Rieke, G. H., Burrows, A., & Rieke, M. J. 1993, ApJ, 416, 185 (CRBR)
Comerón, F., Rieke, G. H., Claes, P., Torra, J., & Laureijs, R. J. 1998, A&A, 335, 552 (CRCTL)
Comerón, F., Rieke, G. H., & Neuhäuser, R. 1999, A&A, 343, 477
D'Antona, F., & Mazzitelli, I. 1994, ApJS, 90, 467 (DM94)
————. 1997, Mem. Soc. Astron. Italiana, 68, 823 (DM97)
Dolidze, M. V., & Arakeylan, M. A. 1959, Soviet Astron., 3, 434
Elias, J. H. 1978, ApJ, 224, 453
Elias, J. H., Frogel, J. A., Matthews, K., & Neugebauer, G. 1982, AJ, 87, 1029
Grasdalen, G. L., Strom, K. M., & Strom, K. E. 1973, ApJ, 184, L53
Greene, T. P., & Lada, C. J. 1996, AJ, 112, 2184
————. 1997, AJ, 114, 2157
Greene, T. P., & Meyer, M. R. 1995, ApJ, 450, 233
Greene, T. P., Wilking, B. A., André, P., Young, E. T., & Lada, C. J. 1994, ApJ, 434, 614
Greene, T. P., & Young, E. T. 1992, ApJ, 395, 516
Hartmann, L., & Kenyon, S. J. 1996, ARA&A, 34, 207
Herbig, G. H. 1998, ApJ, 497, 736
Hillenbrand, L. A. 1997, AJ, 113, 1733
Humphreys, R. M., Jones, T. J., & Sitko, M. L. 1984, AJ, 89, 1155
Kenyon, S. J., Brown, D. I., Tout, C. A., & Berlind, P. 1998a, AJ, 115, 2491
Kenyon, S. J., & Hartmann, L. 1995, ApJS, 101, 117
Kenyon, S. J., Lada, E. A., & Barsony, M. 1998b, AJ, 115, 252
Kirkpatrick, J. D., Henry, T. J., & Irwin, M. J. 1997, AJ, 113, 1421
Kirkpatrick, J. D., et al. 1999, ApJ, 519, 802
Kleinmann, S. G., & Hall, D. N. B. 1986, ApJS, 62, 501
Lada, C. J. 1987, in Star-forming Regions, ed. M. Peimbert & J. Jugaku (Dordrecht: Reidel), 1
Lada, C. J., & Adams, F. C. 1992, ApJ, 393, 278
Lada, C. J., & Wilking, B. A. 1984, ApJ, 287, 610
Leggett, S. K. 1992, ApJS, 82, 351
Leous, J. A., Feigelson, E. D., André, P., & Montmerle, T. 1991, ApJ, 379, 683

Luhman, K. L. 1998, in ASP Conf. Ser. 134, Brown Dwarfs and Extrasolar Planets, ed. R. Rebolo, E. L. Martín, & M. R. Zapatero-Osorio (San Francisco: ASP), 532
————. 1999, ApJ, in press
Luhman, K. L., Briceño, C., Rieke, G. H., & Hartmann, L. W. 1998a, ApJ, 493, 909
Luhman, K. L., Liebert, J., & Rieke, G. H. 1997, ApJ, 489, L165
Luhman, K. L., & Rieke, G. H. 1998, ApJ, 497, 354 (LR)
Luhman, K. L., Rieke, G. H., Lada, C. J., & Lada, E. A. 1998b, ApJ, 508, 347 (LRLL)
Martín, E. L., Montmerle, T., Gregorio-Hetem, J., & Casanova, S. 1998, MNRAS, 300, 733
Martín, E. L., Rebolo, R., & Zapatero Osorio, M. R. 1996, ApJ, 469, 706
Meyer, M. R. 1995, Ph.D. thesis, Univ. Massachusetts
Meyer, M. R., Calvet, N., & Hillenbrand, L. A. 1997, AJ, 114, 288
Miller, G. E., & Scalo, J. M. 1979, ApJS, 41, 513
Montmerle, T., Koch-Miramonde, L., Falgarone, E., & Grindlay, J. E. 1983, ApJ, 269, 182
Motte, F., André, P., & Neri, R. 1998, A&A, 336, 150
Muzerolle, J., Calvet, N., & Hartmann, L. 1998, ApJ, 492, 743
Myers, P. C., Fuller, G. A., Mathieu, R. D., Beichman, C. A., Benson, P. J., Schild, R. E., & Emerson, J. P. 1987, ApJ, 319, 340
Najita, J., Carr, J. S., Glassgold, A. E., Shu, F. H., & Tokunaga, A. T. 1996, ApJ, 462, 919
Reid, I. N., et al. 1999, ApJ, submitted
Rieke, G. H., Ashok, N. M., & Boyle, R. P. 1989, ApJ, 339, L71
Rieke, G. H., & Lebofsky, M. J. 1985, ApJ, 288, 618
Rieke, G. H., & Rieke, M. J. 1990, ApJ, 362, L21
Salpeter, E. E. 1955, ApJ, 121, 161
Scalo, J. 1986, Fundam. Cosmic Phys., 11, 1
————. 1998, in ASP Conf. Ser. 142, The Stellar Initial Mass Function, 38th Herstmonceux Conference, ed. G. Gilmore, I. Parry, & S. Ryan (San Francisco: ASP), 201
Shu, F. H., Adams, F. C., & Lizano, S. 1987, ARA&A, 25, 23
Simon, M., et al. 1995, ApJ, 443, 625
Stahler, S. W. 1983, ApJ, 274, 822
Strom, K. M., Kepner, J., & Strom, S. E. 1995, ApJ, 438, 813
Strom, K. M., & Strom, S. E. 1994, ApJ, 424, 237
Struve, O., & Rudkjøbing, M. 1949, ApJ, 109, 92
Testi, L., & Sargent, A. I. 1998, ApJ, 508, L91
Tokunaga, A. T., & Kobayashi, N. 1999, AJ, 117, 1010
Vrba, F. J., Strom, K. M., Strom, S. E., & Grasdalen, G. L. 1975, ApJ, 197, 77
Vrba, F. J., Strom, S. E., & Strom, K. M. 1976, AJ, 81, 958
Wainscoat, R. J., Cohen, M., Volk, K., Walker, H. J., & Schwartz, D. E. 1992, ApJS, 83, 111
Wallace, L., & Hinkle, K. 1996, ApJS, 107, 312
Whittet, D. C. B. 1974, MNRAS, 168, 371
Wilking, B. A., Greene, T. P., & Meyer, M. R. 1998, AJ, 117, 469 (WGM)
Wilking, B. A., & Lada, C. J. 1983, ApJ, 274, 698
Wilking, B. A., Lada, C. J., & Young, E. T. 1989, ApJ, 340, 823
Wilking, B. A., Schwartz, R. D., & Blackwell, J. H. 1987, AJ, 94, 106
Williams, D. M., Comerón, F., Rieke, G. H., & Rieke, M. J. 1995, ApJ, 454, 144
Williams, D. M., Thompson, C. L., Rieke, G. H., & Montgomery, E. F. 1993, Proc. SPIE, 1308, 482
Young, E. T., Lada, C. J., & Wilking, B. A. 1986, ApJ, 304, L45